SIMULATING THE MECHANICAL RESPONSE OF TITANIUM ALLOYS THROUGH THE CRYSTAL PLASTICITY FINITE ELEMENT ANALYSIS OF IMAGE-BASED SYNTHETIC MICROSTRUCTURES

A Thesis

Presented in Partial Fulfillment of the Requirements for the Degree
Master of Science in the Graduate School of The Ohio State
University

By

Josh Thomas, B.S.

Graduate Program in Mechanical Engineering

The Ohio State University

2012

Master's Examination Committee:

Somnath Ghosh, Advisor

June Key Lee

Reji John

Report Documentation Page	*Form Approved* *OMB No. 0704-0188*

1. REPORT DATE **2012**	2. REPORT TYPE	3. DATES COVERED **00-00-2012 to 00-00-2012**

4. TITLE AND SUBTITLE **Stimulating The Mechanical Response Of Titanium Alloys Through The Crystal Plasticity Finite Element Analysis Of Image-Based Synthetic Microstructures**	5a. CONTRACT NUMBER 5b. GRANT NUMBER 5c. PROGRAM ELEMENT NUMBER
6. AUTHOR(S)	5d. PROJECT NUMBER 5e. TASK NUMBER 5f. WORK UNIT NUMBER
7. PERFORMING ORGANIZATION NAME(S) AND ADDRESS(ES) **The Ohio State University,Columbus,OH,43210**	8. PERFORMING ORGANIZATION REPORT NUMBER
9. SPONSORING/MONITORING AGENCY NAME(S) AND ADDRESS(ES)	10. SPONSOR/MONITOR’S ACRONYM(S) 11. SPONSOR/MONITOR’S REPORT NUMBER(S)

12. DISTRIBUTION/AVAILABILITY STATEMENT

Approved for public release; distribution unlimited

13. SUPPLEMENTARY NOTES

14. ABSTRACT

15. SUBJECT TERMS

16. SECURITY CLASSIFICATION OF:			17. LIMITATION OF ABSTRACT	18. NUMBER OF PAGES	19a. NAME OF RESPONSIBLE PERSON
a. REPORT **unclassified**	b. ABSTRACT **unclassified**	c. THIS PAGE **unclassified**	**Same as Report (SAR)**	**103**	

Standard Form 298 (Rev. 8-98)
Prescribed by ANSI Std Z39-18

Abstract

Micromechanical crystal plasticity finite element simulations of the response of synthetic titanium microstructures are carried out with the goal of quantifying the effect of microstructure on mechanical properties. Two separate materials are studied: (1) an α-β Ti-6Al-4V material and (2) a highly-textured, rolled α Ti-3Al-2.5V sheet material. Performing accurate finite element analyses begins with accurate image-based characterization of the morphological and crystallographic features of the materials at the microstructural scale. Then, statistically equivalent representative 3D microstructures are built and meshes are generated for crystal plasticity based finite element method (CPFEM) analysis. For the Ti-3Al-2.5V material, experimental results from the displacement controlled mechanical testing of dog bone shaped, rolled specimens are used for the calibration of elastic parameters as well as anisotropic crystal plasticity parameters. The inspection of micrographs of the rolled material showed elongated grain shapes which led to the updating of the crystal plasticity model to include grain aspect ratio dependence on the Hall-Petch size effect–an update of a previous size effect model which assumed spherical grains. Model validation is achieved by comparing load controlled experimental results with simulated creep results. For the Ti-6Al-4V material, the robust and validated analysis tool is used to perform sensitivity analyses and a quantitative understanding of how individual microstructural parameters affect the mechanical response properties of the alloy is developed. Functional dependencies are proposed that directly connect the metal's microstructural features to creep response, yield strength response, and tensile response.

Acknowledgments

I would like to acknowledge and thank my advisor, Dr. Somnath Ghosh, for investing in me and hiring me when I had been away from engineering for a number of years and for the valuable technical training he has given me the past 2 years. I count it a privilege to have benefited in multiple ways from his exceptional expertise and accomplishments in this field. In addition, I am thankful for his continued support through some potentially difficult circumstances. He went out of his way to ensure that I was supported to the very end.

Dr. Mike Groeber deserves special acknowledgement for his time and efforts in personally helping me with my project during these entire 2 years. Dr. Masoud Anahid, as well as my lab mates, especially Dr. Pritam Chakraborty also deserve acknowledgement. Probably not a day went by without an insightful technical discussion with one of them. I owe a lot of my training in computational mechanics to their willingness to help and mentor me even through times where they had their own work to do.

I would be remiss in not giving a special acknowledgement to Dr. Reji John because he not only served on my committee and gave insightful input on this manuscript, but he also graciously hosted me at AFRL/RX on a number of occasions. My visits to AFRL/RX and the interactions with Dr. John's group there

added a unique dimension and depth to this work as well as my education. In particular, Mr. John Porter, Dr. Dennis Buchanan, and Mr. Phil Blosser of the University of Dayton Research Institute deserve acknowledgement for the characterization and testing of the Ti-3Al-2.5V performed at AFRL/RX. Also, the photographs presented in this work were taken by them and a few of the schematics were either given by them or inspired by them.

Special thanks to Brian Welk from Dr. Hamish Fraser's group in MSE at OSU for help with characterization of the Ti-6Al-4V. I would also like to thank Dr. June Lee for taking the time to serve on my committee.

This work has been sponsored in part by the US National Science Foundation (Grant # CMMI-0800587, Program Manager: Dr. Clark Cooper) and the ONR/DARPA D3D Project (Grant # N00014-05-1-0504, Program Manager: Dr. Julie Christodoulou). Additional sponsorship was provided by the Air Force Research Laboratory, Materials and Manufacturing Directorate (AFRL/RX, Metallic Thermal Protection System Program, Universal Technology Corporation/AFRL Grant, Program Managers: Todd Warren and Reji John).

Computer support by the Ohio Supercomputer Center through grant # PAS813-2 is also acknowledged.

Vita

2004	B.S. Aerospace Engineering, The Ohio State University
2010-present	Graduate Research Associate, The Ohio State University.

Fields of Study

Major Field: Mechanical Engineering

Table of Contents

List of Tables

List of Figures

Chapter 1: Introduction

Titanium alloys are widely used in a number of applications spanning a range of industries including the aerospace, medical, and even sporting goods industries [25]. The positive properties of titanium, including high strength to weight ratio, good fracture toughness, and good corrosion resistance make this material desirable. One downside to titanium alloys, however, is that they exhibit a "cold" creep phenomena where time-dependent deformation, which is normally observed at elevated temperatures in most alloys, is seen to occur at room temperature and at loads as low as 60% of yield strength [38, 39, 28, 20, 29, 35, 43, 15]. The "cold" creep mechanism, being at low homologous temperatures, is not diffusion-mediated, but occurs due to dislocation glide where dislocations are arrayed in a planar fashion. This planarity of slip has been attributed to the effect of short range ordering of Ti and Al atoms on the hcp lattice [29].

More recent research has shown the "cold" creep response is strongly dependent on crystallographic orientation in titanium [38, 1]. Ghosh et al. have developed CPFEM models for analyzing the time-dependent mechanical response of representative titanium microstructures [14, 7, 42]. These models are capable of capturing the anisotropic creep response of realistic titanium microstructures with a large number of grains (on the order of 1000 grains). In particular, the most recent models are able to treat the more complex transformed β colony regions consisting of alternating layers of both hcp and bcc phases. One goal of this current work is to study the anisotropic creep response of these relatively complicated bimodal titanium alloys.

It is well known that the microstructural features of polycrystalline materials directly affect mechanical properties (including the creep response described above). However, much of the understanding of the relationships between microstructure and properties is qualitative. One approach to developing more quantitative understanding is through generating large quantities of different microstructures through different heat treatments and thermomechanical processing. Then, through testing of these samples, large databases of experimental results are populated and, through neural network fuzzy logic modeling, functional dependency relationships are created [40, 6, 23]. In addition to the large cost associated with processing and testing real samples, one of the downsides to this experimental approach is that it is very difficult to vary one microstructural feature while holding the others constant during heat treatment processing because the evolution of most of these important features is highly coupled.

Another method for determining microstructure-property relationships is through sensitivity studies performed using crystal plasticity based finite element method (CPFEM) analyses of synthetic microstructures. This method is pursued in the current work. One of the beneficial aspects of this approach is that a large array of synthetic samples with different microstructural features can be generated and tested at a low cost compared with testing of real specimen. Furthermore, in contrast to the limitations when generating real samples, it is possible to vary the microstructural features of these synthetic samples independently in order to gain a more direct understanding of their effect on properties. This approach is not without its own difficulties and drawbacks, which include the need for calibration and validation of the models and large amounts of computing power. However, there have been recent advances in the validation and robustness of CPFEM models (as discussed above) and one goal of the current work (see Chapter 3) is to add to the robustness of the calibration and validation of these models. Furthermore, the increased availability of the computing power necessary to solve high resolution CPFEM problems with a large number of grains means computational simulation has a lot to offer towards the solution to this problem. In [41], the sensitivity of yield strength to phase volume fraction was studied using synthetic microstructures consisting of cubic grains. In the current work, more realistic grain morphologies are used and a fuller set of response parameters has been studied including not just yield strength, but also creep parameters and Ramberg-Osgood parameters.

The process for developing a quantitative understanding of microstructure-property relationships using CPFEM analyses begins with the detailed characterization of microstructural features of real titanium samples. This process consists of 2D microstructure characterization, 3D microstructure model creation, meshing and CPFEM. Post-processing of the CPFEM results give stress-strain curves and creep curves whose parameters can be determined and then studied with respect to changes in microstructural features. The quantitative characterization of material microstructure is the crucial first step in this process. This task is accomplished through SEM image analysis, EBSD data collection, stereological procedures and statistical quantification. Once the characterization data sets are acquired, a 3D reconstruction code described in [8] is used to create a statistically equivalent, synthetic microstructure which is meshed and used in computational simulation. Results are compared with experimental test results and the model is validated. Finally, an array of synthetic microstructures with varying statistics is generated and analyzed to gain an understanding of response sensitivities. See Figure 1.1 for a flowchart that portrays the full methodology and process described in the current work.

Various aspects of this process were carried out using two separate but related materials and the work with these two materials is described in the following 2 chapters: Chapter 2 describes work based on the α-β Ti-6Al-4V material, and Chapter 3 describes work done based on the α Ti-3Al-2.5V material.

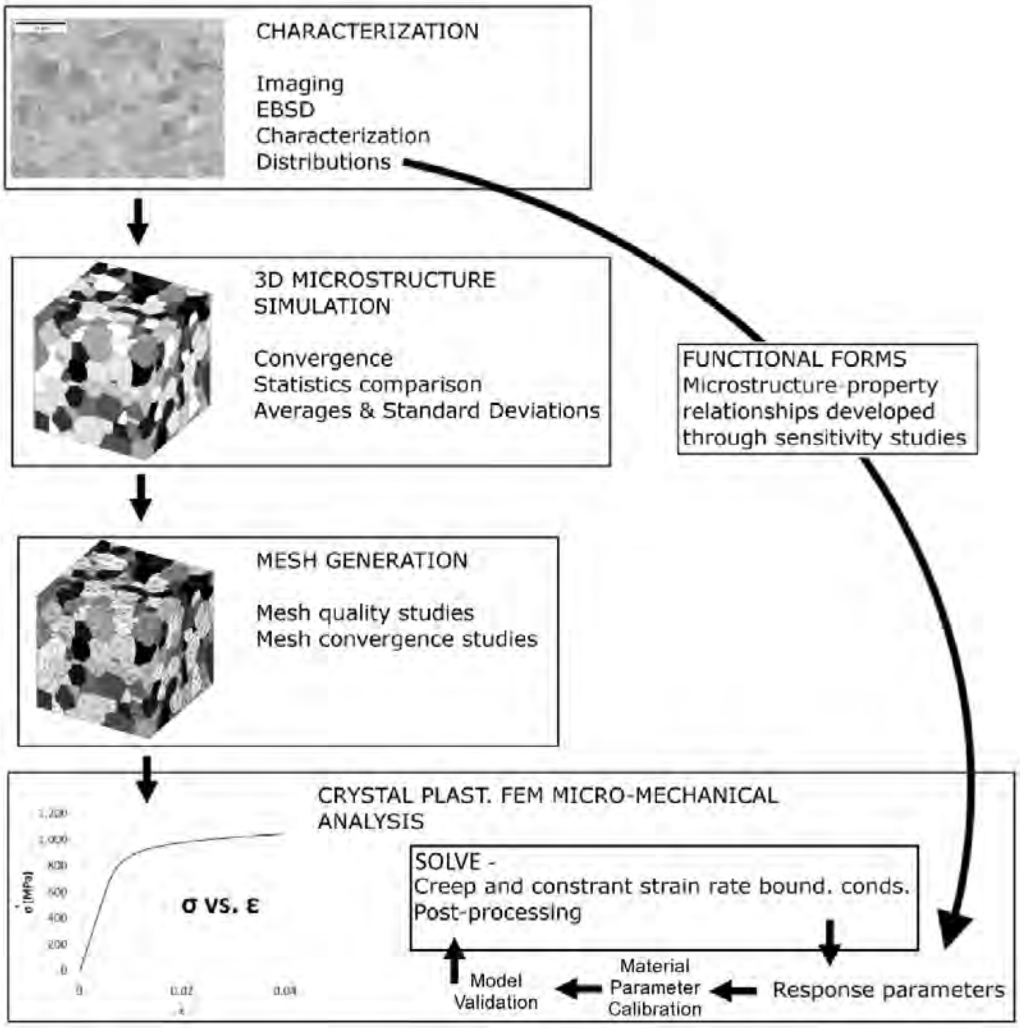

Figure 1.1: Flowchart of modeling methodology and process.

Chapter 2: Ti-6Al-4V Material

This chapter describes work done based on the α-β Ti-6Al-4V material. Micrograph images and EBSD scans of the pre-tested material and a yield strength experimental data point from a mechanical test of a real sample provided a basis for developing the computational model and proposed functional forms connecting microstructure to mechanical properties. The proposed model which connects α lath thickness to yield strength is validated against a previously published linear regression model generated from the testing of 75 separate Ti-6Al-4V samples with various heat treatment histories.

2.1 CPFEM Simulation of Polycrystalline Ti-6Al-4V

In order to accurately simulate the micromechanical response of polycrystalline materials, it is important to develop both a good microstructure model as well as a good micromechanical model. These separate but related aspects to the simulation are discussed in the following pages beginning with the microstructural simulation model.

2.1.1 3D Polycrystalline Microstructural Simulation and Mesh Generation

The following section discusses the 2D characterization and generation of 3D microstructure models from the 2D data. It has been shown that 3D microstructures are able to be collected by a number of techniques, such as Focused Ion Beam (FIB) sectioning [10], manual polishing [33] and x-ray methods [22], but all remain somewhat tedious and time consuming and have not progressed to a point where they are feasible in this type of sensitivity study. Rather, the work presented here will employ an extrapolation process of estimating 3D statistics from 2D measurements. This area, known as stereology, has been a source of ongoing investigation for years [34], and will serve in conjunction with more recent direct 3D techniques, to inform the process used in this work.

Microstructural Characterization of the α-β Ti-6Al-4V

To complete the microstructural characterization of the α-β Ti-6Al-4V, micrographs of the Ti-6Al-4V material were analyzed and statistics were compiled. One of the micrographs analyzed is shown in Figure 2.1. The microstructure consists of 2 major regions: (1) transformed β colonies consisting of alternating α laths (hcp) and β ribs (bcc) and (2) equiaxed primary α grains (hcp).

Schematics of the hcp and bcc unit cell crystal structure and slip systems based on atomic packing are shown in Figures 2.2 and 2.3. The hcp crystal has an non-orthogonal basis while the bcc crystal has an orthogonal basis.

The crystallographic orientations of this material are influenced by the β-to-α phase transformation, which generally obeys the Burger's orientation relationship and the resultant material has a misorientation distribution with preferences to certain

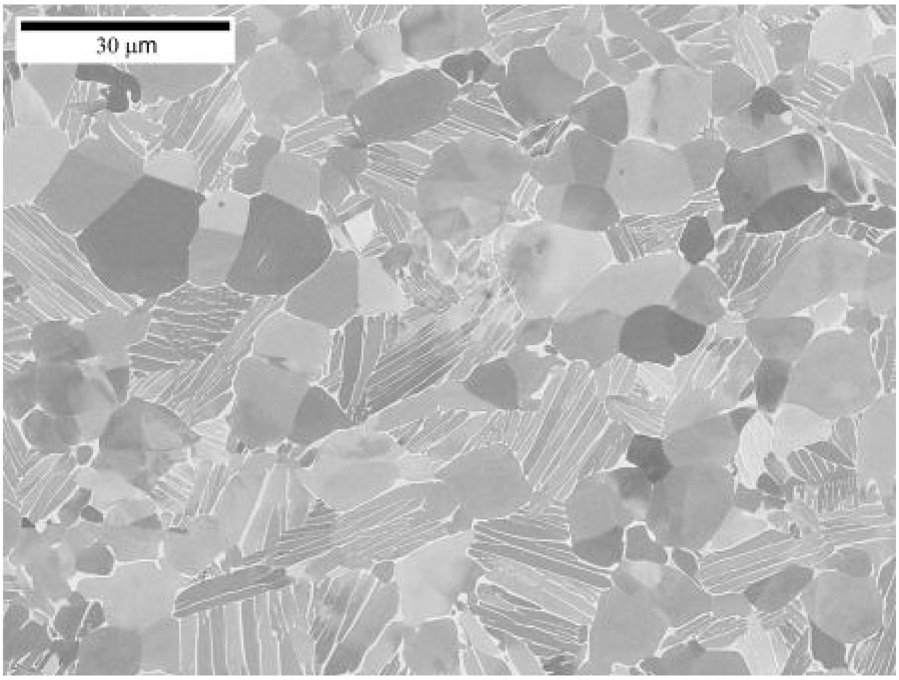

Figure 2.1: One of 7 images at 1000X magnification.

variants [32]. Figure 2.6 shows the misorientation distribution (MoDF) of the sample used in this work. The MoDF is comparable to that seen in the Ti-6Al-4V work done by Randle in 2008 [32].

The sample was imaged using an FEI Sirion SEM. A number of images were acquired using this microscope; including three sets of seven images at magnifications of 750X, 1000X, and 1500X. Figure 2.1 shows one of the images taken at 1000X magnification. These images were analyzed and, using the stereological techniques and assumptions described in [36] the data shown in Table 2.1 were collected. These particular morphological features are considered by experimentalists to be among the most important features of these alloys that directly affect the response [23, 18].

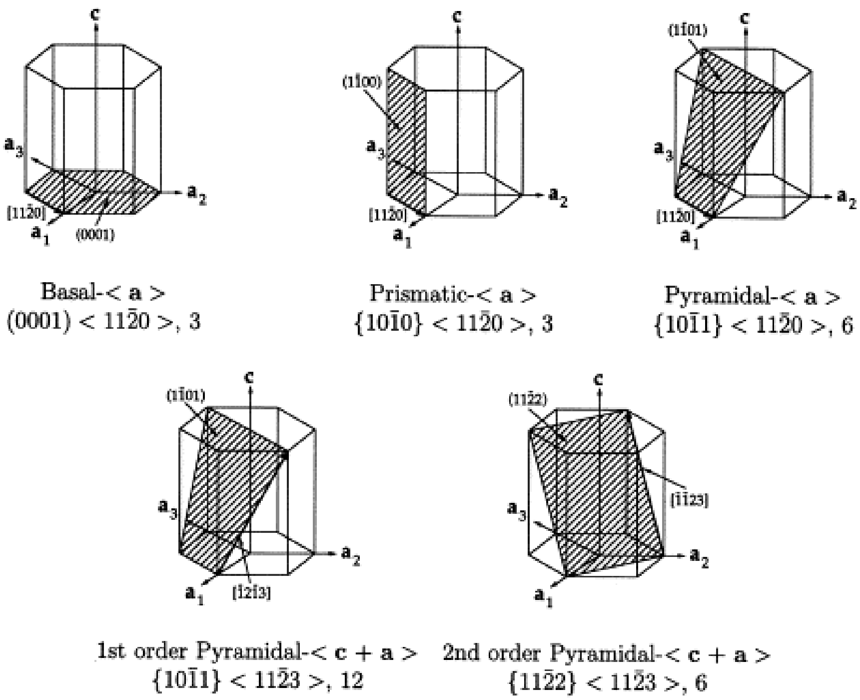

Basal-< **a** > $(0001) < 11\bar{2}0 >$, 3

Prismatic-< **a** > $\{10\bar{1}0\} < 11\bar{2}0 >$, 3

Pyramidal-< **a** > $\{10\bar{1}1\} < 11\bar{2}0 >$, 6

1st order Pyramidal-< **c** + **a** > $\{10\bar{1}1\} < 11\bar{2}3 >$, 12

2nd order Pyramidal-< **c** + **a** > $\{11\bar{2}2\} < 11\bar{2}3 >$, 6

Figure 2.2: Hcp crystal structure and slip systems with non-orthogonal basis. Figure taken from Balasubramanian [1].

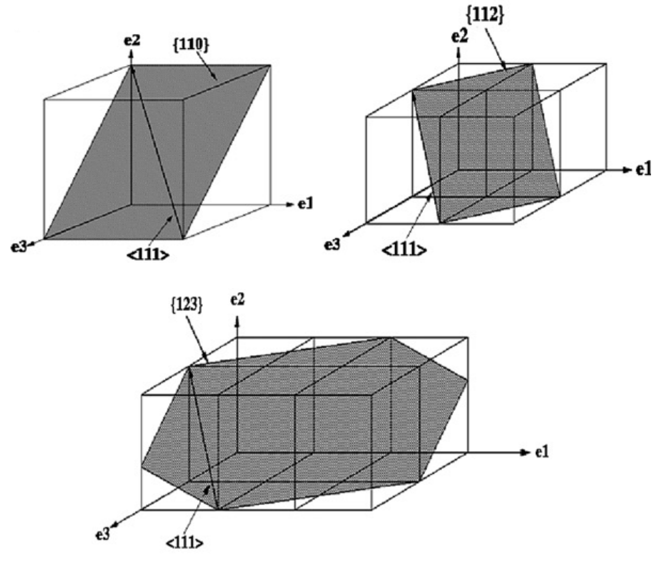

Figure 2.3: Bcc crystal structure and slip systems with orthogonal basis. Figure taken from Venkatramani [42].

Param.	Description	Value
D	average grain/col. size ($\overline{ESD}$)	11.9 μm
S^{sd}	stand. dev. grain/col. size	5.22 μm
l_α	α lath thickness	0.29 μm
l_β	β rib thickness	0.089 μm
V_f	vol. fract. of glob. α phase	49.9 %
V_{fT}	vol. fract. of total α phase	93 %

Table 2.1: Morphological data determined from SEM images and stereology.

Grain/colony size is defined by the equivalent sphere diameter, ESD. ESD is determined by first calculating equivalent circle diameters (ECD) using image analysis techniques along with the assumption that the grains/colonies are spherical in 3D space and therefore their size can be approximated by the following stereological formula which connects the $\overline{ECD}$ of a sample with the $\overline{ESD}$ of a sample:

$$\overline{ESD} = \frac{4}{\pi}\,\overline{ECD}. \tag{2.1}$$

According to [9], the lognormal standard probability density function provides a reasonable fit to the grain/colony size data and this was confirmed for the current work by the testing of approximately 50 standard distributions using a maximum likelihood estimation approach. This function is defined by two parameters, average and standard deviation. For these reasons, the lognormal standard distribution will be used in this work (see Figure 2.4) and will be sampled in the synthetic microstructure generation technique described in the 3D reconstruction section of this paper to produce statistically equivalent synthetic structures.

In addition to the above morphological analysis, the sample of Ti-6Al-4V was analyzed crystallographically. Crystallographic orientation data was obtained through an EBSD scan containing approximately 1000 grains/colonies. The scan was obtained using an FEI Quanta SEM and processed using the code described in [8] to provide hcp orientation data as well as misorientation and microtexture distributions (see Figures 2.5, 2.6, and 2.7 for plots of the data). Misorientation is defined from the 2D EBSD scan along the grain boundary length but assumed as equivalent to a grain boundary surface area in the 3D synthetic structure generation. This assumption is reasonable in that matching is done based on a unitless fraction obtained by normalizing the data by either total grain boundary length (in 2D) or total grain boundary surface area (in 3D). The orientations of the β ribs (which are not directly obtained by the scan because of their small size) are uniquely defined from the Burger's relationship by the orientation of the α phase and the lamellar structure of the transformed β colonies and are incorporated into the CPFEM model based on a mixture rule described in [16].

Microstructural Simulation Procedure

The microstructural simulation is performed using the code described in [8] where statistically equivalent microstructures are generated whose morphological and crystallographic statistics are matched. Although the grains/colonies have been assumed to be spheres for the purpose of characterization, when it comes to generation of the 3D microstructures the grains/colonies are allowed to perturb slightly off sphere with no correlation between the size and shape of grains/colonies. The morphological orientation of the slightly elongated grains/colonies was assumed to be random. Grains/colonies are placed in the synthetic structure based on neighborhood constraints assuming an average number of neighbors to be approximately 14 grains with a variation according to grain size. This choice was based on the analysis of IN100 in [9] in 3D, where it was seen that the number of neighbors of a grain/colony correlated strongly to its size. This assumption of correlation between the number of neighbors of a grain/colony to its size implies a lack of clustering of similarly sized grains/colonies (i.e. random neighborhoods), which appears to be valid when viewing the 2D micrographs. After the morphological voxelized structure has been built, the grains/colonies are assigned hcp orientations based on a random sampling from the ODF. Misorientation and microtexturing statistics are matched by an iterative process where orientations are allowed to switch between grains/colonies or be replaced by new random orientations all the while the error is tracked and compared to sample statistics until convergence is attained.

Microstructural Simulation Validation

The microstructural simulation procedure is validated through comparing the sample statistics with the statistics of the simulated microstructure. Additional validation is achieved through a convergence study of the algorithm. See Figures 2.4, 2.5, 2.6, and 2.7 for graphical comparisons of the sample statistics with a 500-grain synthetically generated 3D microstructure. Good agreement allows us to consider the synthetic structure to be considered statistically equivalent.

The synthetic microstructure generation code can be used to generate structures with any number of grains/colonies. Figures 2.4, 2.5, 2.6, and 2.7 show statistics of a 500-grain/colony structure. It has been seen that by 500 grains/colonies these statistics have converged to a small error as defined by root mean square errors for the average and standard deviation of grain/colony size. The root mean square error for average grain/colony size is defined as:

$$E_{av} = \sqrt{\sum_i \left(A_i^{av} - \overline{ESD}\right)^2} \tag{2.2}$$

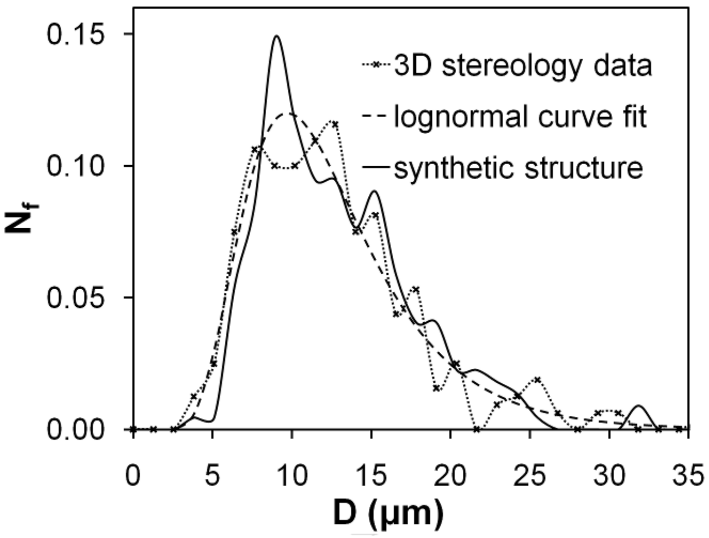

Figure 2.4: Grain/colony size, D, distribution comparison. N_f is the number fraction of grains/colonies.

where A_i^{av} is the average grain/colony size of structures generated with i grains/colonies and $\overline{ESD}$ in this case equals 11.9 μm.

The root mean square error for the standard deviation of grain/colony size is defined as:

$$E_{sd} = \sqrt{\sum_i \left(A_i^{sd} - S^{sd}\right)^2} \tag{2.3}$$

where A_i^{sd} is the standard deviation of grain/colony size of structures generated with i grains/colonies and S^{sd} is the actual standard deviation calculated from the data taken from the EBSD scan which in this case is 5.22 μm. Convergence plots for the synthetic structure generation algorithm show convergence for the matching of the grain/colony size statistics of average and standard deviation (see Figure 2.8). Synthetic structures of less than approximately 300 grains/colonies are seen to not match the statistics very well. Structures of 1000 grains/colonies and above show

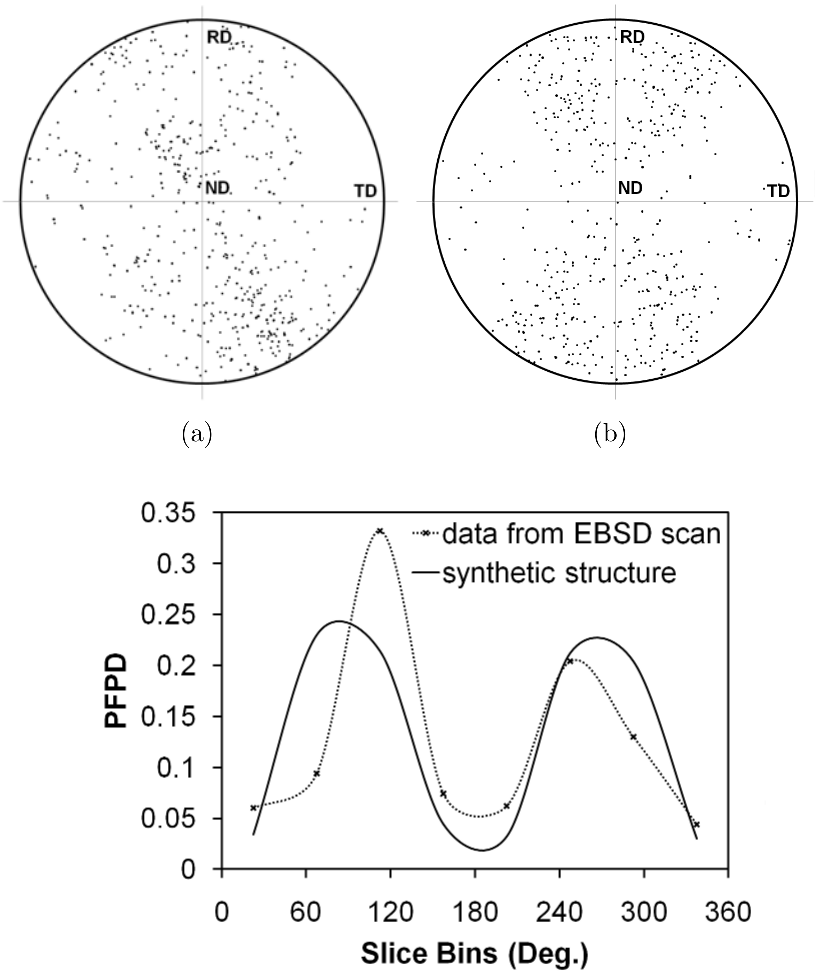

(a)

(b)

(c)

Figure 2.5: α phase (0002) pole figures for (a) Sample data and (b) Synthetic structure as well as (c) pole figure point density (PFPD) distributions of the 2 pole figures for a more quantitative comparison of the crystallographic matching.

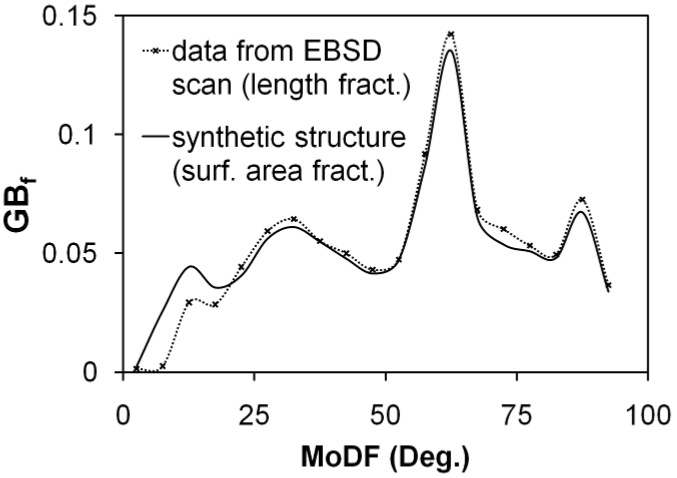

Figure 2.6: Misorientation distribution (MoDF) comparison. GB_f corresponds to either grain/colony boundary length fraction or grain/colony boundary surface area fraction.

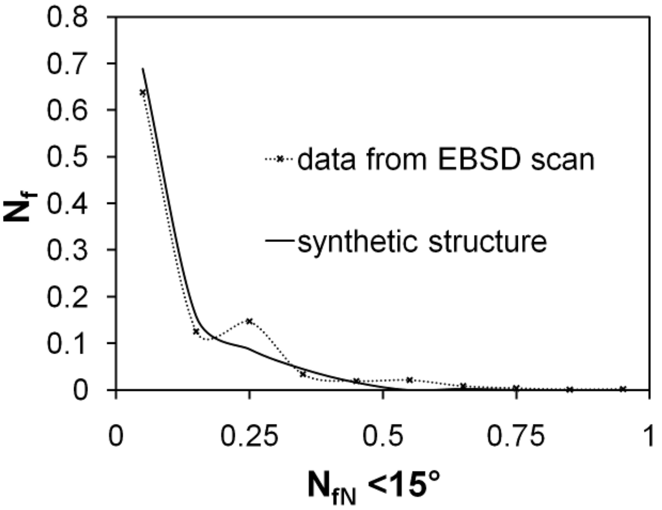

Figure 2.7: Microtexture distribution comparison where microtexture is defined by the number fraction of neighbors (N_{fN}) with misorientation less than 15°. N_f is the number fraction of grains/colonies.

only slight improvement and because larger structures become computationally very expensive, structures of between 500-600 grains/colonies were chosen for the current work.

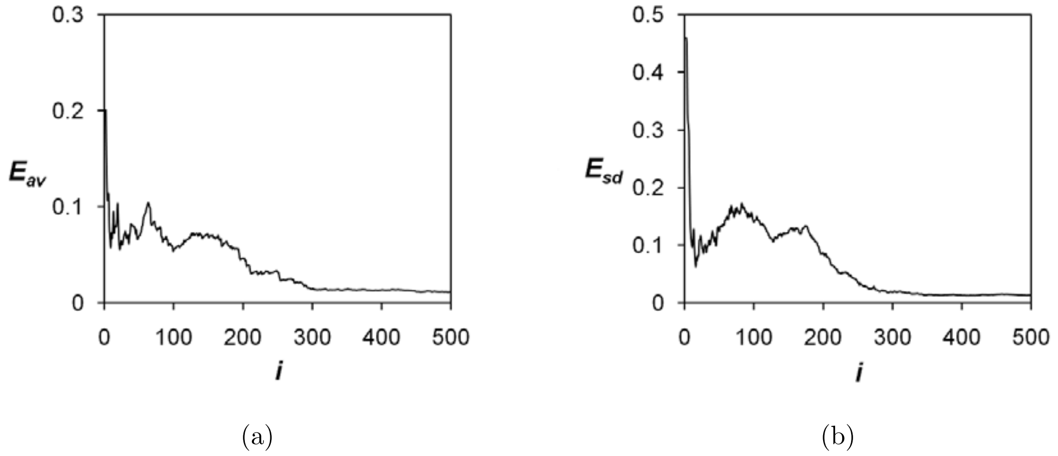

(a)

(b)

Figure 2.8: Convergence Plots: Error of average, E_{av} (a) and Error of standard deviation, E_{sd} (b) of grain/colony size vs. No. of grains/colonies (i) in simulated microstructure.

Mesh Generation

The resultant structure of the 3D microstructure model generation process is a voxelized volume with individual grains/colonies having a phase identification and an orientation defined by 3 Euler angles (see Figure 2.9). This voxelized volume needs to be meshed for finite element analysis. While this structure could be directly transferred into the finite element environment, the voxelized nature of the structure causes a "stair-stepped" boundary between grains/colonies. The "jagged" boundaries have been shown to be the source of local artifacts during simulations [17]. The current work uses the 4-noded TET4 element instead in an attempt to remove the artificial voxelized boundaries.

As this element uses linear interpolation functions, the strains are constant throughout the element and the element is integrated numerically using one point at the centroid of the element. Even though the shape functions for displacement/strain are linear, for the 500 to 600-grain/colony microstructures used for the current work the authors have selected meshes that are refined enough to the end that the creep and constant strain rate responses have converged. In other words, there is little sensitivity of further mesh refinement to response.

The commercial meshing software, Simmetrix [37], is used to generate the finite element mesh (see Figure 2.9). First, a triangular surface mesh is generated along the interior grain boundaries and cube boundaries. Then, this triangular surface element mesh is extended into the full 3D volumetric tetrahedral mesh. The meshes used for the current work contain between approximately 100,000 to 120,000 elements and 20,000 to 22,000 nodes.

The meshes are checked for distorted elements and it has been seen that the meshes used for the current work have a very small number of elements with aspect ratio of 40 or higher (on the order of 0.01%). Because the current work is concerned with the volume average creep and constant strain rate responses, it is reasonable to concede this very small amount of distorted elements.

Two different microstructures were generated that are statistically equivalent: one with 500 grains/colonies and one with 600 grains/colonies. Increasing the number of grains/colonies in the simulated microstructures above 500 shows no affect upon the

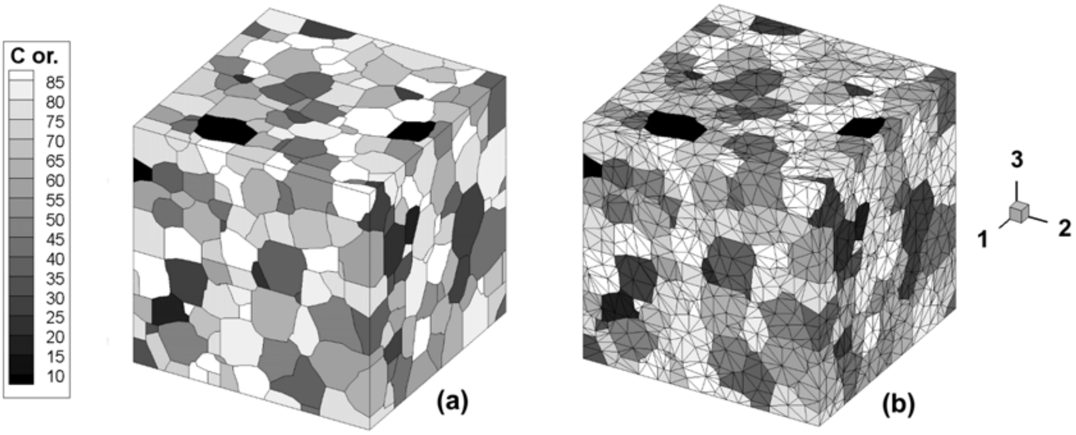

Figure 2.9: Voxelized volume (a) before and (b) after meshing for the 600-grain microstructure. The cube length dimension, l_0, is 68 μm. The grayscale contour variable, C or., is the c-axis orientation defined as the angle between the c-axis of the hcp phase of the grain/colony and the loading direction which in this case is 2.

simulated micromechanical creep response parameters A and m (discussed in Section 2.2). The model has converged with respect to these parameters.

2.1.2 Micromechanical Analysis of Simulated Polycrystalline Microstructures Using a Crystal Plasticity Constitutive Model

An isothermal, size-dependent and rate-dependent crystal plasticity finite element computational model described and developed in [14, 7, 42] is used in conjunction with MSC/Marc Mentat and an in-house parallelized code to simulate the response of the synthetically generated microstructures of the bimodal $\alpha - \beta$ Ti 6Al-4V under various loading and boundary conditions.

Constitutive Model

Crystal deformation is modeled by a combination of elastic stretching and rotation of the crystal and plastic slip on the different slip systems. The stress-strain relation is given in terms of the second Piola-Kirchoff stress ($\mathbf{S} = det\mathbf{F}^e\mathbf{F}^{e-1}\bar{\sigma}\mathbf{F}^{e-T}$) and the work conjugate Lagrange Green strain tensor ($\mathbf{E}^e \equiv (1/2)\left\{\mathbf{F}^{eT}\mathbf{F}^e - \mathbf{I}\right\}$) as,

$$\mathbf{S} = \mathbf{C} : \mathbf{E}^e, \tag{2.4}$$

where C is the fourth-order anisotropic elasticity tensor, $\bar{\sigma}$ is the Cauchy stress tensor, and $\mathbf{F}^e$ is the elastic deformation gradient defined by the relation,

$$\mathbf{F}^e \equiv \mathbf{F}\mathbf{F}^{p-1}, det\mathbf{F}^e > 0. \tag{2.5}$$

$\mathbf{F}$ represents the deformation gradient and $\mathbf{F}^p$ its plastic component. The incompressibility constraint is given by $\det\mathbf{F}^p = 1$. The flow rule describing the plastic deformation is cast in terms of the plastic velocity gradient,

$$L^p = \dot{\mathbf{F}}^p\dot{\mathbf{F}}^{p^{-1}} = \sum_\alpha \dot{\gamma}^\alpha\mathbf{s}_0^\alpha,\ \dot{\gamma}^\alpha = \dot{\tilde{\gamma}}\left|\frac{\tau^\alpha}{g^\alpha}\right|^{1/m} sign(\tau^\alpha), \tag{2.6}$$

where $\dot{\gamma}^\alpha$ is the plastic shearing rate, τ^α is the resolved shear stress, g^α is the slip system deformation resistance (all variables are specified on the αth slip system of the phase). m is a material rate sensitivity parameter and the Schmid tensor, $\mathbf{s}_0^\alpha$, is expressed as

$$\mathbf{s}_0^\alpha \equiv \mathbf{m}_0^\alpha \otimes \mathbf{n}_0^\alpha. \tag{2.7}$$

The slip system deformation resistance, g^α, evolves along with the hardening rates as described in [21, 12] as

$$\dot{g}^\alpha = \sum_{\beta=1}^{nslip} h^{\alpha\beta} \left|\dot{\tilde{\gamma}}^\beta\right| = \sum_\beta q^{\alpha\beta} h^\beta \left|\dot{\gamma}^\beta\right|, \tag{2.8}$$

where $h^{\alpha\beta}$ is the strain hardening rate due to both self and latent hardening, h^β is the self-hardening rate, and $q^{\alpha\beta}$ is a matrix describing the latent hardening. For the hcp α phase, it is assumed that the evolution of the self-hardening rate is governed as

$$h^\beta = h_0^\beta \left|1 - \frac{g^\beta}{g_s^\beta}\right|^r sign\left(1 - \frac{g^\beta}{g_s^\beta}\right), g_s^\beta = \tilde{g}\left(\frac{\dot{\gamma}^\beta}{\dot{\tilde{\gamma}}}\right), \tag{2.9}$$

where h_0^β is the initial hardening rate, g_s^β is the saturation slip deformation resistance, and r, $\tilde{g}$, and n are slip system hardening parameters. A different relation is used for the evolution for the bcc β phase found in transformed β colonies as follows:

$$h^\beta = h_s^\beta + sech^2\left[\left(\frac{h_0^\beta - h_s^\beta}{\tau_s^\beta - \tau_0^\beta}\right)\gamma^\alpha\right](h_0^\beta - h_s^\beta), \gamma_\alpha = \int_0^t \sum_{\beta=1}^{nslip} \left|\dot{\gamma}^\beta\right| dt, \tag{2.10}$$

where h_0^β and h_s^β are the initial and asymptotic hardening rates, τ_s^β represent the saturation value of the shear stress when $h_s^\beta = 0$, and γ_α is a measure of total plastic shear.

In continuum plasticity, the dependence of the yield stress on the grain size has been expressed by Hall and Petch in the 1950s [11, 30]. A Hall-Petch-type equation is used in the crystal plasticity formulation. This equation relates the initial slip system deformation resistance, g^α, to a characteristic size as

$$g^\alpha = g_0^\alpha + \frac{K^\alpha}{\sqrt{D^\alpha}}, \tag{2.11}$$

where g_0^α and K^α are size-effect-related slip system constants that refer to the initial slip system deformation resistance and slope, respectively, and D^α is the characteristic length scale governing the size effect (see Section 3.2.2 for a grain aspect ratio dependence model update on this size effect). According to work done in [42], the transformed β regions have D^{α} values which correspond either to the colony size, the α lath thickness, or β rib thickness depending on ease of slip conditions at the hcp-bcc interfaces of the colony lath structure. For primary α grains, the D^{α} values are assumed to be the ESD of the grain.

Material Properties

Elasticity and crystal plasticity parameters are implemented and calibrated from a multi-variable optimization method developed and carried out in [13] and [7] where α Ti-6Al single crystals and $\alpha-\beta$ Ti-6242 single colonies were experimentally tested. Tables 2.3 and 2.2 give the elastic parameters for both the hcp and bcc phases. Tables 2.4, 2.5, and 2.6 give the calibrated values of the plastic parameters for both the hcp and bcc phases in the transformed β colonies as well as the hcp parameters for the primary α grains. An implicit backward Euler time-integration scheme is used for the solution to the dynamic problem using the commercial finite element code, MSC/Marc Mentat [27] along with the user-defined material routine UMAT.

C_{ij} parameter	Value (GPa)
C_{11}=C_{22}	170.0
C_{33}	204.0
C_{12}=C_{21}	98.0
C_{13}=C_{31}=C_{23}=C_{32}	86.0
C_{44}	C_{11}-C_{12}
C_{55}=C_{66}	102.0
Other C_{ij}	0

Table 2.2: Calibrated elastic parameters of the transversely isotropic tensor for the hcp phase.

C_{ij} parameter	Value (GPa)
C_{11}=C_{22}=C_{33}	250.21
C_{13}=C_{31}=C_{23}=C_{32}=C_{12}=C_{21}	19.0
C_{44}=C_{55}=C_{66}	230.65
Other C_{ij}	0

Table 2.3: Calibrated elastic parameters of the cubic symmetric tensor for bcc phase.

Parameters for Slip System	m	g_0 (MPa)	$\dot{\tilde{\gamma}}(s^{-1})$	h_0	h_s	τ_0 (MPa)	τ_s (MPa)
{101}	0.02	450.00	0.0023	1500.0	25.0	500.0	200.0
{112} soft	0.02	429.82	0.0023	1371.6	25.0	500.0	200.0
{112} hard	0.02	409.63	0.0023	1979.8	25.0	500.0	200.0
{123} soft	0.02	451.28	0.0023	2312.0	25.0	500.0	200.0
{123} hard	0.02	400.67	0.0023	1634.8	25.0	500.0	200.0

Table 2.4: Calibrated parameters for the *bcc* slip systems in the homogenized transformed β colonies.

Parameters for Slip System	m	g_0 (MPa)	$\dot{\tilde{\gamma}}(s^{-1})$	h_0	r	$\tilde{\gamma}$ (MPa)	n (MPa)
Basal a_1	0.02	284.0	0.0023	1500.0	0.30	450.0	0.14
Basal a_2	0.02	315.0	0.0023	2300.0	0.30	634.0	0.10
Basal a_3	0.02	243.0	0.0023	8000.0	0.40	371.0	0.05
Prismatic a_1	0.02	240.0	0.0023	3450.0	0.29	504.0	0.15
Prismatic a_2	0.02	210.0	0.0023	6500.0	0.20	583.0	0.25
Prismatic a_3	0.02	240.0	0.0023	3600.0	0.30	504.0	0.15
Pyr. <a>	0.02	395.0	0.0023	100.0	0.10	550.0	0.01
Pyr. <c+a>	0.02	623.3	0.0023	100.0	0.10	1650.0	0.01

Table 2.5: Calibrated parameters for the *hcp* basal <a> and prismatic <a> slip systems in the homogenized transformed β colonies.

Parameters for Slip System	m	g_0 (MPa)	$\dot{\tilde{\gamma}}(s^{-1})$	h_0	r	$\tilde{\gamma}$ (MPa)	n (MPa)
Basal <a>	0.02	284.00	0.0023	100.0	0.1	450.0	0.01
Prism. <a>	0.02	282.24	0.0023	100.0	0.1	550.0	0.01
Pyr. <a>	0.02	395.00	0.0023	100.0	0.1	550.0	0.01
Pyr. <c+a>	0.02	623.30	0.0023	100.0	0.1	1650.0	0.01

Table 2.6: Calibrated parameters for the slip systems in the primary α grains.

Boundary and Loading Conditions

For both the constant strain rate and creep simulations to suppress rigid body modes, symmetric constraint conditions are applied where the back faces of the cube are constrained as u_1=0 on the 1-face, u_2=0 on the 2-face, and u_3=0 on the 3-face. The cube is free to move in all other directions. For constant strain rate simulations, one of the outer faces is given a constant strain rate displacement boundary condition of $u_{ii}(t) = l_0(exp(\dot{\epsilon}_{ii}^c t) - 1)$, where l_0 is the initial dimension of the cube and $\dot{\epsilon}_{ii}^c$ is the applied constant strain rate with i corresponding to which direction the cube is being loaded in. For creep simulations, a constant load is applied to one of the outer faces.

2.2 Comparison of the CPFEM Model with Experimental Results

The CPFEM model results are compared with the experimental data available for the tested specimen. One data point was available; that being the engineering yield strength (YS=821 MPa) as defined by a 0.2% strain offset method for a tensile experiment conducted at a strain rate of $10^{-4}s^{-1}$. Post-processing of the solution gives the engineering stress-strain curve and the simulated yield strength (YS) is determined to be 833 MPA (based on the 2% strain offset method) with a small g_0^α parameter calibration (10% reduction required) deemed reasonable because parameters were not originally calibrated for this particular alloy. This YS value is compared with the experimental value of 821 MPA. The error is 1.5% after the slight calibration. The entire stress-strain curve determined by the simulation can be seen in Figure 2.10. This result is encouraging considering the limited 2D data that was available for characterization of the material.

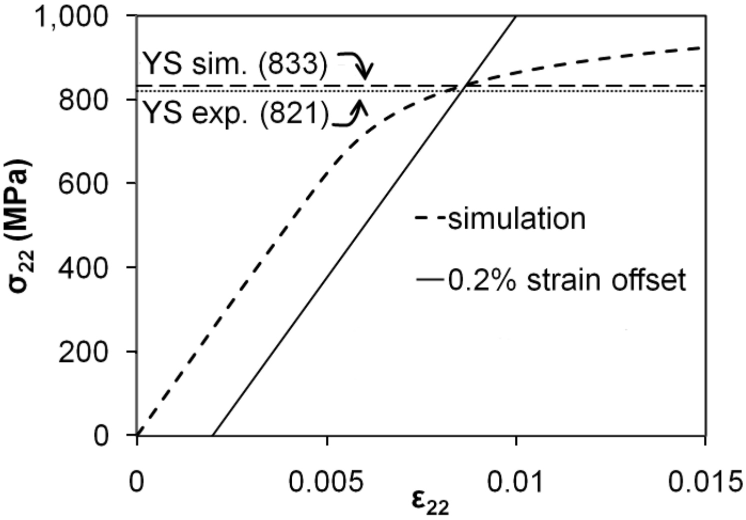

Figure 2.10: Engineering stress-strain response with comparison of simulated YS and experimental YS. The 2-direction is the loading direction.

Figure 2.11 shows 1 of the many internal grains before and after creep loading at 700 MPa (approx. 83% of yield strength) for 10,000 sec. The contour variable, ϵ_p, is plastic strain. The deformation is scaled by a factor of 50.

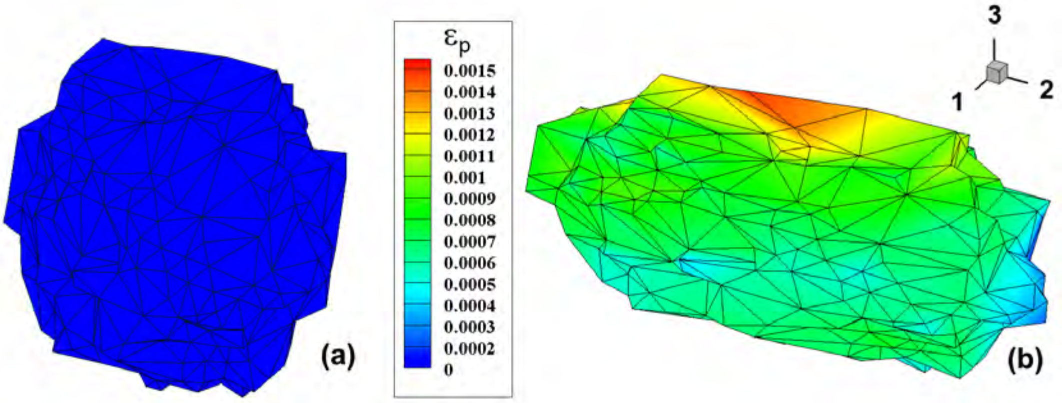

Figure 2.11: A single internal grain in its (a) undeformed and (b) deformed state after creep loading in the 2-direction at 700 MPa for 10,000 sec. The deformation is scaled by a factor of 50 and the contour variable, ϵ_p, is plastic strain.

2.3 Microstructure-Dependent Macroscopic Models for Yield Strength, Creep and Constant Strain Rate Behavior

Much advance has been made towards developing microstructure-property relationships for titanium alloys through the use of neural network models [40, 6, 18, 19, 44]. However, the time and cost that is associated with building those neural network models can be quite significant. They are expensive to develop in that they require the population of a huge database of experimental data to be useful. Furthermore, in order to train the neural network, the experiments need to be performed on samples that have microstructural features that span a wide range of values. To achieve this variation in microstructure, it is necessary to perform expensive highly controlled heat treatments on the material before testing. Additionally, because of the strong interrelationship between microstructural features such as grain/colony size and α lath size, it is essentially impossible through experimental means to vary only one microstructural feature in order to investigate its effect on mechanical properties [23]. The computational tools and methods discussed and implemented here provide an alternative which helps to overcome these limitations. Sensitivity studies have been performed in the current work to lay the groundwork for proposed functional forms that relate microstructural features to mechanical properties.

2.3.1 Definition of Model Response Parameters

Although the CPFEM micromechanical model defines the deformation gradient as $\mathbf{F} \equiv \mathbf{F^e F^p}$, for describing the stress-strain curves, true strain is additively decomposed into its elastic and plastic portions as $\epsilon = \epsilon_e + \epsilon_p$. It is understood that this assumption does not hold well for values of large strain; however, this inaccuracy is deemed acceptable for the current work where parameters are fit using simulation data that falls mainly in the smaller strain regions. The Ramberg-Osgood equation [31] is given as:

$$\epsilon = \frac{\sigma}{E} + K(\frac{\sigma}{E})^n, \tag{2.12}$$

where the first term represents the elastic portion of the strain, ϵ_e and the second term represents the plastic portion of the strain, ϵ_p. K and n are two dimensionless material parameters. Post processing in crystal plasticity distinguishes the plastic strain from the total strain and curves are fit to determine the K and n material response parameters. These parameters provide a good description of the constant strain rate response of the material.

For describing the creep response, a power creep law given by Lubahn and Felgar is used [24] where again the true strain is decomposed into its elastic and plastic portions and the plastic portion of the response is given by

$$\epsilon_p = At^m, \tag{2.13}$$

where t is time, and A (with units of 1/sec) and m (which is dimensionless) are material constants which are fit to the creep simulation results. Again, it is acknowledged that the additive decomposition does not hold well for large strain problems but this inaccuracy is accepted based on the fact that most of the simulation fitting is in a smaller strain regime.

2.3.2 Sensitivity Studies

In this study, an array of synthetic specimens is produced and studied and sensitivities of response to changes in microstructural features are reported. A realistic reference microstructure is used and, one by one, each feature is varied while all other features are held constant. The current work studies the sensitivity of response to variations in α lath size, l_α, β rib size, l_β, volume fraction of primary α grains, V_f, and average grain/colony size, D. As discussed above, this is a unique capability that is not available through experimental means. The response values that are studied include yield strength, the Ramberg-Osgood parameters K and n (see Eqn. 2.12), and the power creep law parameters A and m (see Eqn. 2.13). The following figures show sensitivities of these microstructural features to YS (Figures 2.12-2.15), as well as power creep law parameters, A (Figures 2.16-2.19) and m (Figures 2.20-2.23), and Ramberg-Osgood parameters, K (Figures 2.24-2.27) and n (Figures 2.28-2.31).

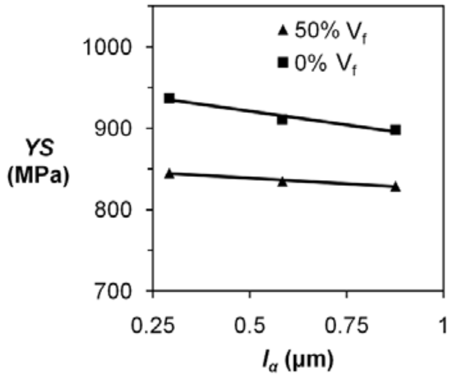

Figure 2.12: Sensitivity of yield strength (YS) to changes in α lath thickness (l_α).

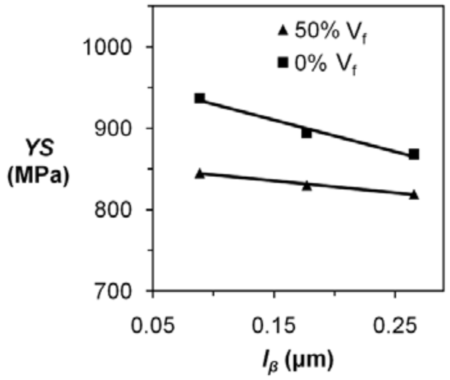

Figure 2.13: Sensitivity of yield strength (YS) to changes in β rib thickness (l_β).

The studied range of α lath thicknesses and the corresponding β rib thicknesses from approximately 0.2 to 1.0 μm and 0.1 to 0.3 μm are realistic ranges. Experimentally, ranges that cover sizes differing by 500% are easily attained in real samples by varying processing cooling rates [23].

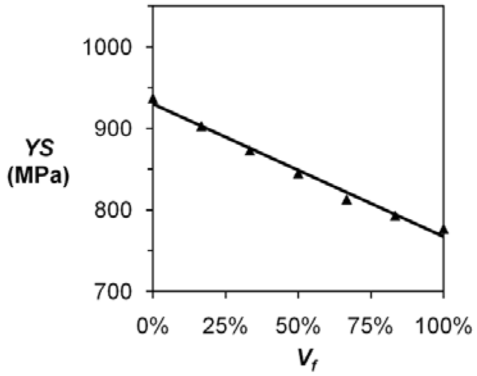

Figure 2.14: Sensitivity of yield strength (YS) to changes in volume fraction of primary α (V_f).

Simulation results show that in general changes to l_α and l_β have a smaller effect on response compared to the larger effects seen from changes in V_f and D. The relatively smaller affect of these feature sizes on response can be explained by the fact that V_f and D are relatively larger features and therefore it is expected that variations in these features would have a relatively greater affect on the response.

As seen in Figures 2.12 and 2.13 (as well as the other figures which investigate the sensitivities of l_α and l_β), the results for a 0% V_f sample were also investigated. The 0% V_f cases correspond to a 100% transformed β colony sample. As would be expected, there is a greater sensitivity to changes in l_α and l_β for the 0% V_f cases

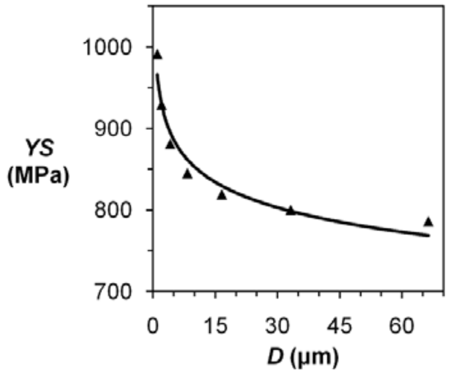

Figure 2.15: Sensitivity of yield strength (YS) to changes in average grain/colony size (D).

compared to the 50% V_f cases. This is explained by the fact that the primary α grains have no lath or rib structure. In other words, the fewer of these pure-α grains in the structure and the more of the colony structure the higher the effect of changes to the lath and rib thicknesses.

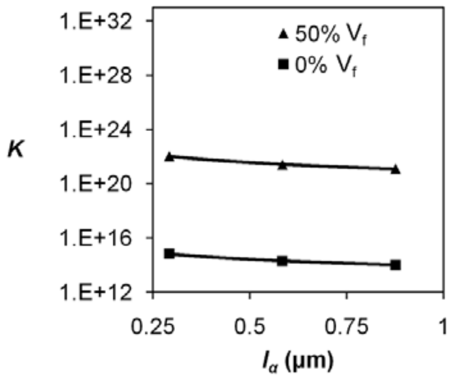

Figure 2.16: Sensitivity of K parameter to changes in α lath thickness (l_α).

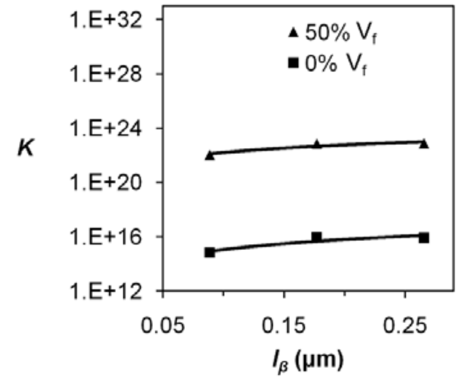

Figure 2.17: Sensitivity of K parameter to changes in β rib thickness (l_β).

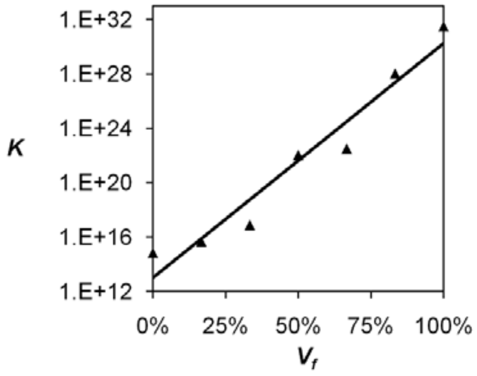

Figure 2.18: Sensitivity of K parameter to changes in volume fraction primary α (V_f).

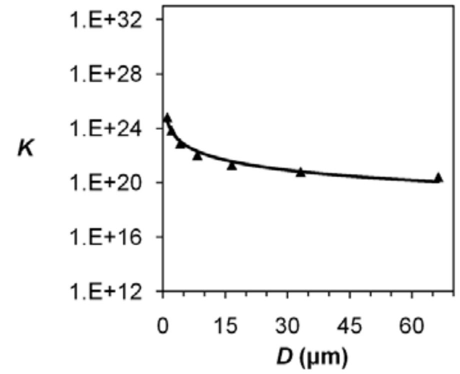

Figure 2.19: Sensitivity of K parameter to changes in grain/colony size (D).

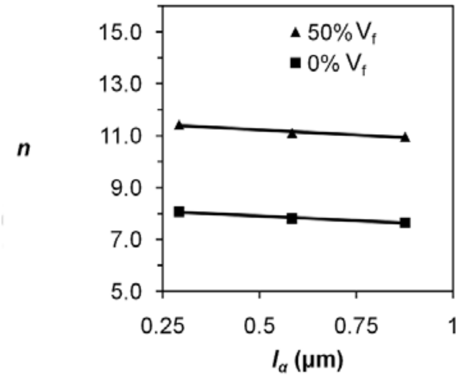

Figure 2.20: Sensitivity of n parameter to changes in α lath thickness (l_α).

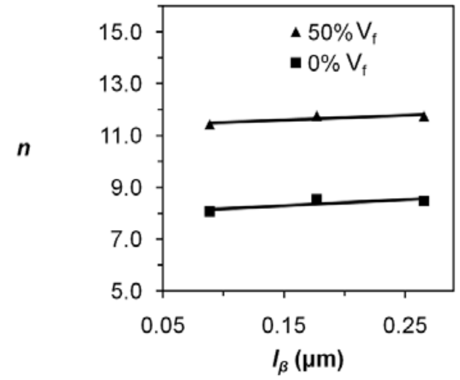

Figure 2.21: Sensitivity of n parameter to changes in β rib thickness (l_β).

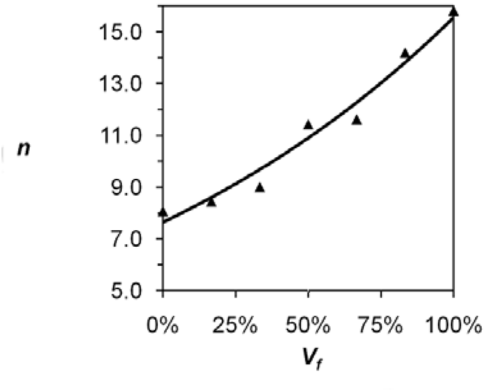

Figure 2.22: Sensitivity of n parameter to changes in volume fraction primary α (V_f).

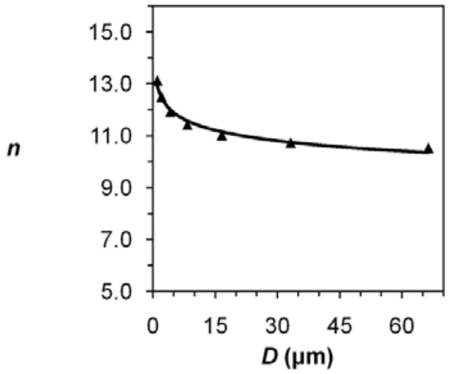

Figure 2.23: Sensitivity of n parameter to changes in grain/colony size (D).

Focusing on the sensitivity of YS to the various microstructural features (Figures 2.12-2.15), the trend is consistent for all features that as more grain/colony boundary or more lath/rib boundary is introduced into the structure the YS increases. This trend is in agreement with the understanding that boundaries impede dislocation motion and therefore hinder the onset of plastic deformation and ultimately increase the strength of a material.

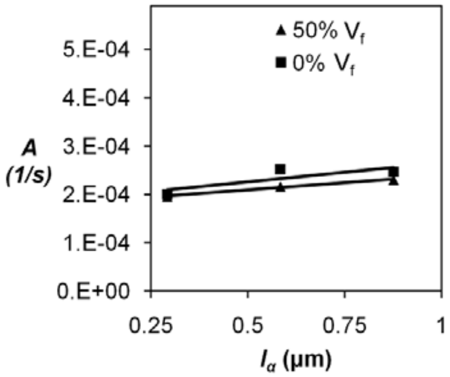

Figure 2.24: Sensitivity of A parameter to changes in α lath thickness (l_α).

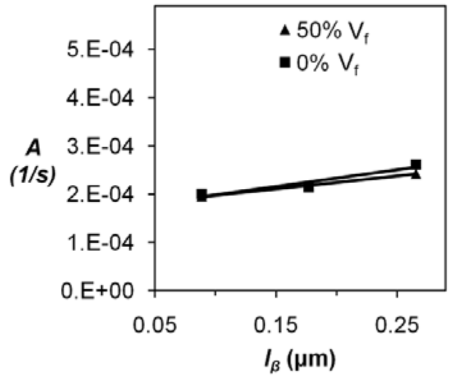

Figure 2.25: Sensitivity of A parameter to changes in β rib thickness (l_β).

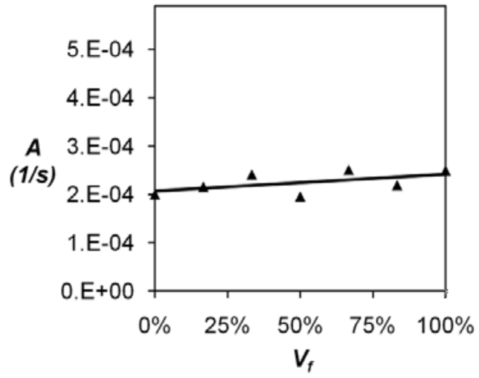

Figure 2.26: Sensitivity of A parameter to changes in volume fraction primary α (V_f).

It is also worth taking note of the sensitivity of YS to average grain/colony size (Figure 2.15). This non-linear response shows a Hall-Petch-type relationship where initially (with smaller grain sizes) there is a very large sensitivity to changes in grain/colony size, D, and then as D become larger and larger there is a saturation and there is not as much sensitivity to increases in D after it reaches around 20 μm.

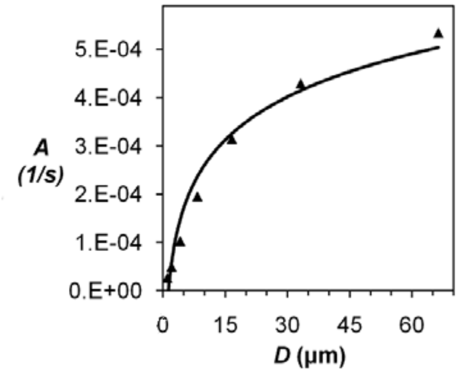

Figure 2.27: Sensitivity of A parameter to changes in grain/colony size (D).

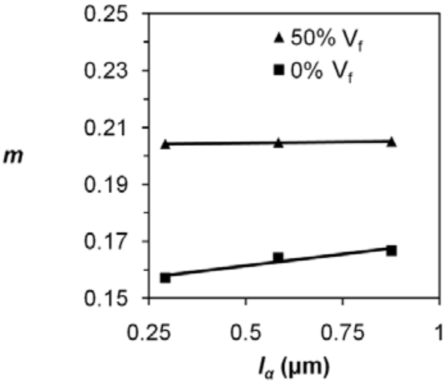

Figure 2.28: Sensitivity of m parameter to changes in α lath thickness (l_α).

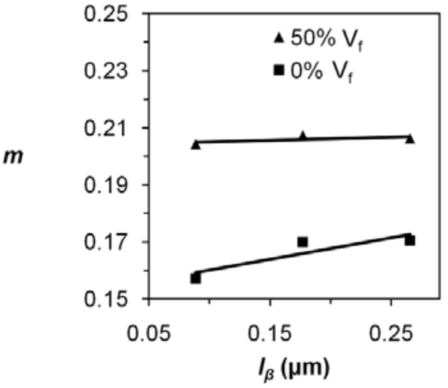

Figure 2.29: Sensitivity of m parameter to changes in β rib thickness (l_β).

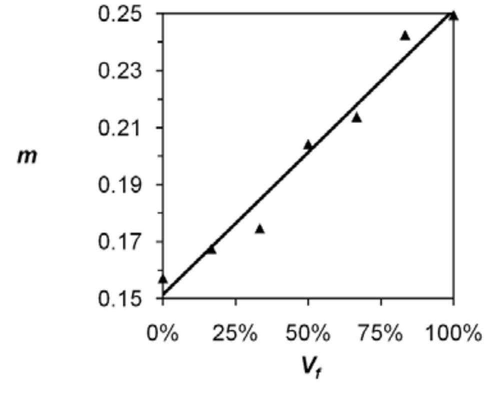

Figure 2.30: Sensitivity of m parameter to changes in volume fraction primary α (V_f).

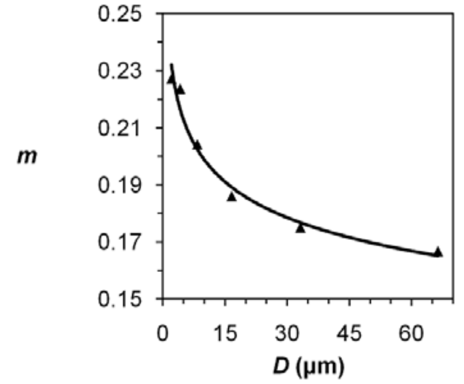

Figure 2.31: Sensitivity of m parameter to changes in grain/colony size (D).

These results are comparable with the experimental results seen by Yoshimura and Nakahigashi [45]. They have obtained grain sizes as small as 1 μm in α-β Ti using hydrogen treatments and saw that YS results followed the Hall-Petch relationship well at these values. A common two-parameter version of the Hall-Petch relationship is given as,

$$YS = \sigma_0 + \frac{K^*}{\sqrt{D}} \tag{2.14}$$

where σ_0 and K^* (not to be confused with the K parameter of the Ramberg-Osgood equation used in this work) are macroscopic size-effect constants.

Plotting the YS as a function of $1/D^{0.5}$ (Figure 2.32), a value of σ_0 of 760 MPa and K^* of 240 MPa$\sqrt{\mu\text{m}}$ are obtained from a straight line fit. These values are compared to those obtained by [42] for a synthetic specimen of Ti-6242 of 750 MPa and 250 MPa$\sqrt{\mu\text{m}}$ respectively.

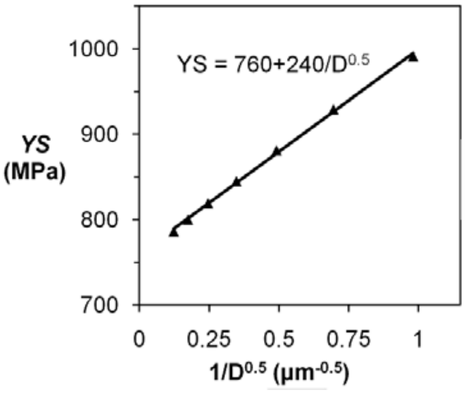

Figure 2.32: Hall-Petch two parameter model.

Focusing our attention to Figures 2.15, 2.19, 2.23, 2.27, and 2.31, the effect of average grain size, D, on all the response parameters can be compared. Notice that, just like for YS, the K and n parameters, as well as the creep parameters, A and m show the similar characteristic of high sensitivity at low grain sizes and a lessened sensitivity as grain size increases. In future work, it could be examined if for a very large average grain size the effect of changes in alpha lath and beta rib thickness would be heightened.

2.3.3 Functional Forms

Full functional forms that connect microstructural features and material response parameter are developed using the sensitivity information discussed in the previous section. The forms are developed assuming that variational effects are independent of each other.

The yield strength, YS, as a function of α lath thickness, l_α, β rib thickness, l_β, volume fraction of primary α, V_f, and average grain/colony size, D, is determined to be

$$YS(l_\alpha, l_\beta, V_f, D) = k_{YS} * YS(l_\alpha) * YS(l_\beta) * YS(V_f) * YS(D), \tag{2.15}$$

where $YS(l_\alpha) = -27.4 * l_\alpha + 852$, $YS(l_\beta) = -147 * l_\beta + 857$, $YS(V_f) = -163 * V_f + 930$, $YS(D) = 968 * D^{-0.055}$, and k_{YS} is a calibrated constant which equals 1.62E-9.

A validation of the proposed functional form connecting l_α to YS is obtained by comparison with previously published work. In 2002, Tiley [40] developed a linear regression model based off neural network modeling of experimental yield strength results from approximately 75 different Ti-6Al-4V samples that had been heat treated to produce different α lath thicknesses. Tiley's linear regression model obtained from a large amount of experimental data provides a good validation for the proposed functional form connecting YS to l_α. The linear regression model obtained from experiments given by Tiley as, $YS(l_\alpha) = -15.4 * l_\alpha + 826$, (MPa), is compared with the model proposed here from simulations of $YS(l_\alpha) = -27.4 * l_\alpha + 852$, (MPa). Figure 2.33 gives a plot comparing the two linear regression models.

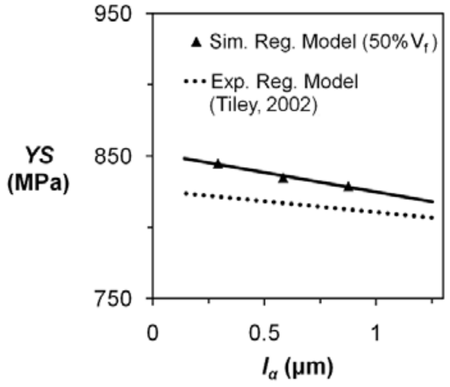

Figure 2.33: Comparison of the linear regression model obtained from experiment [40] and that obtained from simulation for YS vs. l_α.

The Ramberg-Osgood parameter, K, as a function of α lath thickness, l_α, β rib thickness, l_β, volume fraction of primary α, V_f, and average grain/colony size, D, is determined to be

$$K(l_\alpha, l_\beta, V_f, D) = k_K * K(l_\alpha) * K(l_\beta) * K(V_f) * K(D), \tag{2.16}$$

where $K(l_\alpha) = 9.44E20 * l_\alpha^{-1.97}$, $K(l_\beta) = 1.21E24 * l_\beta^{1.88}$, $K(V_f) = 1.03E13 * e^{39.7*V_f}$, $K(D) = 3.89E24 * D^{-2.48}$, and k_K is a calibrated constant which equals 9.22E-67.

The Ramberg-Osgood parameter, n, as a function of α lath thickness, l_α, β rib thickness, l_β, volume fraction of primary α, V_f, and average grain/colony size, D, is determined to be

$$n(l_\alpha, l_\beta, V_f, D) = k_n * n(l_\alpha) * n(l_\beta) * n(V_f) * n(D), \tag{2.17}$$

where $n(l_\alpha) = -0.794 * l_\alpha + 11.6$, $n(l_\beta) = 1.82 * l_\beta + 11.3$, $n(V_f) = 7.65 * e^{0.710 * V_f}$, $n(D) = 13.0 * D^{-0.00536}$, and k_n is a calibrated constant which equals 6.24E-4.

The creep parameter, A, as a function of α lath thickness, l_α, β rib thickness, l_β, volume fraction of primary α, V_f, and average grain/colony size, D, is determined to be

$$A(l_\alpha, l_\beta, V_f, D) = k_A * A(l_\alpha) * A(l_\beta) * A(V_f) * A(D), \tag{2.18}$$

where $A(l_\alpha) = 5.95E - 05 * l_\alpha + 1.80E - 04$, $A(l_\beta) = 2.66E - 04 * l_\beta + 1.71E - 04$, $A(V_f) = 3.50E - 05 * V_f + 2.07E - 04$, $A(D) = 1.29E - 04 * ln(D) - 3.57E - 05$, and k_A is a calibrated constant which equals 9.59E10.

The creep parameter, m, as a function of α lath thickness, l_α, β rib thickness, l_β, volume fraction of primary α, V_f, and average grain/colony size, D, is determined to be

$$m(l_\alpha, l_\beta, V_f, D) = k_m * m(l_\alpha) * m(l_\beta) * m(V_f) * m(D), \tag{2.19}$$

where $m(l_\alpha) = 1.49E - 03 * l_\alpha + 2.04E - 01$, $m(l_\beta) = 1.11E - 02 * l_\beta + 2.04E - 01$, $m(V_f) = 9.98E - 02 * V_f + 1.51E - 01$, $m(D) = 2.49E - 01 * D^{-9.81E-02}$, and k_m is a calibrated constant which equals 1.18E02.

2.3.4 An Extended Investigation of Material Anisotropy

With a validated and calibrated CPFEM model, the material anisotropy is investigated by loading a synthetic microstructure with similar statistics in different directions. In addition to the experimental loading direction (i=2), the response of the synthetic structure to loadings in the other 2 orthogonal directions (i=1,3) is also considered. The constant strain rate results shown in Figure 2.34 confirm the anisotropy. This anisotropy is a direct result of the non-random grain orientations and the anisotropy in the parameters which govern the elastic-plastic response of the individual slip systems.

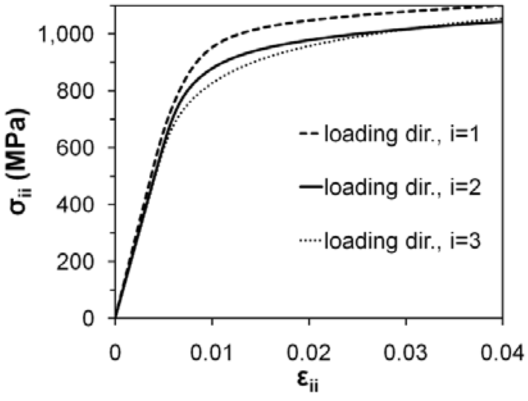

Figure 2.34: Simulated engineering stress-strain response for loadings in 3 directions (i=1,2,3).

The anisotropy of the microstructure under different loading directions can be characterized by the softness index. The softness index is a dimensionless parameter defined as,

$$SI \equiv SF^s * YS/g_0^s, \tag{2.20}$$

where SF^s is the schmid factor of the softest slip system of the grain/colony (which depends on the loading direction and the slip plane normal direction of the softest slip system), YS is the macroscopic yield strength of the entire sample, and g_0^s is the size-dependent initial slip system resistance of the softest slip system of the grain/colony. Figure 2.35 shows the distribution of softness index for the three loading direction cases (i=1,2,3). Softness index values of 1 or higher indicate that the grain/colony will plastically deform when the applied load reaches YS while values below 1 indicate that the grain/colony will not see any plastic deformation at YS. Notice that loading directions i=2 and i=3 have more "softer" grains/colonies compared to case i=1. This explains the "harder" response of loading direction i=1 seen in Figure 2.34.

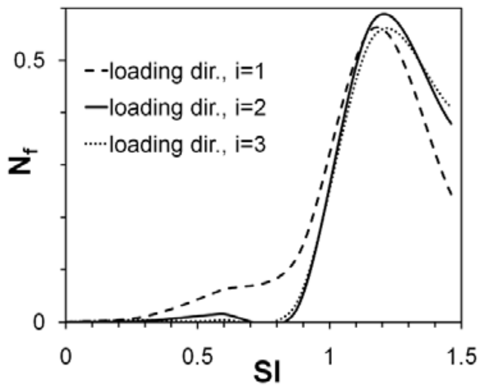

Figure 2.35: Distribution of softness index (SI) for the three loading directions (i=1,2,3). N_f is the number fraction of grains/colonies. Notice that loading dir. i=1 has fewer "softer" grains/colonies.

To further investigate anisotropy, modified versions of the Ramberg-Osgood equation 2.12 and power creep law equation 2.13 are used to characterized the anisotropy in the constant strain rate and creep response. The Ramberg-Osgood equation is modified to include a dependence on loading direction and response direction as,

$$\epsilon_{jj} = \frac{\sigma_{ii}}{E_{ii}} + K^i_{jj}(\frac{\sigma_{ii}}{E_{ii}})^{n^i_{jj}}, \tag{2.21}$$

where i is the loading direction and j is the response direction. The power creep law equation is modified as well as,

$$\epsilon_{pjj} = A^i_{jj} t^{m^i_{jj}}, \tag{2.22}$$

where i is the loading direction and j is the response direction.

Three creep simulations were run at approximately 75-90% of yield strength at a constant load of 700 MPa for 10,000 sec for the three orthogonal loading directions. The following tables (Tables 2.7, 2.8 and 2.9) summarize the simulation results for the three loading directions. Notice the anisotropy between the three cases.

load dir.		i=1	
resp. dir.	jj=11	jj=22	jj=33
YS (MPa)	917	n/a	n/a
K	3.9E37	-9.0E36	-2.4E35
n	18.7	18.6	17.8
A (1/s)	2.3E-04	-8.8E-05	-1.4E-04
m	0.136	0.145	0.130

Table 2.7: Simulation and model fit results showing anisotropy (loading dir.: i=1).

load dir.		i=2	
resp. dir.	jj=11	jj=22	jj=33
YS (MPa)	n/a	853	n/a
K	-2.2E-27	4.3E27	-8.1E25
n	14.2	14.1	13.3
A (1/s)	-8.4E-05	1.8E-04	-1.0E-04
m	0.171	0.205	0.223

Table 2.8: Simulation and model fit results showing anisotropy (loading dir.: i=2).

The highly anisotropic plastic response of this material with its dependence on grain orientation is consistent with expectations because it is well known that Ti alloys show this property due to the low symmetry of the predominant hcp α phase [42]. The values here for m range between 0.136 to 0.223, which is consistent with experimentally determined values of approximately 0.2 for Ti-6Al-4V. According to

load dir.		i=3	
resp. dir.	jj=11	jj=22	jj=33
YS (MPa)	n/a	n/a	786
K	-5.0E16	-5.4E17	9.8E17
n	9.0	9.4	9.4
A (1/s)	-2.5E-04	-3.0E-04	5.5E-04
m	0.160	0.178	0.173

Table 2.9: Simulation and model fit results showing anisotropy (loading dir.: i=3).

Chu [4], these values for Ti-6Al-4V are significantly larger than those observed for other metals and alloys at low homologous temperatures. This implies that creep exhausts extraordinarily slowly in Ti alloys which, in general, is not good for engineering applications. An understanding of how to minimize this property in Ti alloys is important and is facilitated by the quantitative understanding given in this work of how microstructure affects this "cold" creep phenomenon.

Chapter 3: Ti-3Al-2.5V TPS Material

The Space Shuttles used for NASA's recently retired Space Shuttle program were built with a Thermal Protection System (TPS) to withstand heating during atmospheric reentry. The partially reusable system was composed mainly of ceramic tiles and blankets designed to be used for multiple missions, but with a large amount of refurbishment required between launches. In order to drastically reduce the cost of any future reusable launch vehicle systems, metallic TPS will need to be developed. There has been a focus in recent years for developing these metallic systems to the end of reducing the cost of space access [3, 2].

One challenge associated with developing these metallic TPS is accurately determining the mechanical properties of thin metallic foil materials in the range of 75-250 μm. In [26], Morrissey et al. describe a test system that has been developed that has advanced the state-of-the-art in testing capabilities for these thin sheets of material. For the current work, this test system was used to provide a large amount of experimental data for different specimens of thin-gage rolled Ti-3Al-2.5V. Though the most likely selection for a titanium metallic TPS alloy is a high temperature capable material such as Ti-6Al-2Mo-4Zr-2Sn, the readily available Ti-3Al-2.5V commercial alloy was selected as a suitable substitute material to demonstrate the effect of cold rolling on the texture of the processed material and the corresponding anisotropic mechanical response of the sheet.

Following a similar process described in Chapter 2, the following chapter describes the modeling work completed using the mechanical response experimental data as well as the micrographs and EBSD scans of the pre-tested material. Because of the pronounced effect of the rolling on the material's microstructure and the large amount of test data for specimens of different orientations, the calibration and validation of the highly anisotropic material parameters for this material were able to be completed with a good degree of fidelity.

3.1 Experimental Set-up and Results

In comparison with the experimental data available for the Ti-6Al-4V material used in Chapter 2, for this material an abundance of experimental data was available for model comparison, calibration, and validation. Using a newly developed test system for mechanical characterization of thin metallic foils discussed by Morrissey et al. in [26], mechanical response data for a number of foil specimens was provided. See Figure 3.5 for a picture of the experimental set-up.

Foil sample specimens were taken from the bulk sheet material cut to be aligned with both the rolling direction (RD specimens) and the transverse direction (TD specimens). See Figure 3.1 for a schematic. On these individual specimens, strain gages were attached to collect local strain data in both the axial direction (0° strain gages) and transverse direction (90° strain gages). Some tests included 45° strain gages. See Figure 3.2 for a schematic showing the strain gage placements. A schematic of a typical foil specimen with dimensions is shown to scale in Figure 3.3. Thicknesses of the foil specimens are 4.5 MIL (approximately 120 μm). See Figure 3.4 for a close-up picture of one of the experimental specimens showing strain gage placement for the 0° and 90° strain gages. Notice wires running to the back side of the specimen; the reverse side of the specimens have a similar strain gage set-up. This was on account of the thin nature of the specimens in order to confirm that applied displacements and loads were not causing any warping of the specimen in out-of-plane directions. Similar front and back strain gage measurements confirmed a well-executed test.

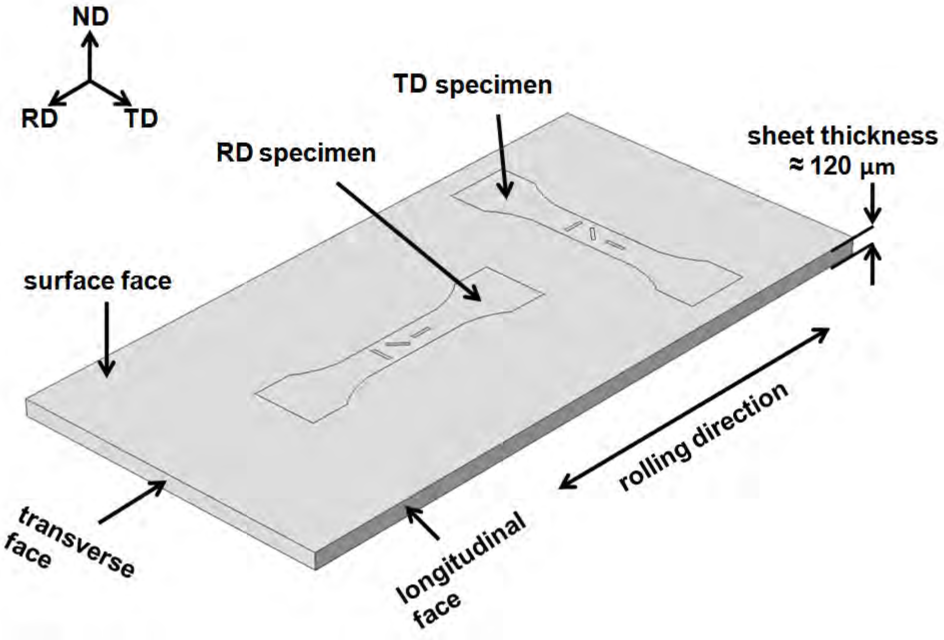

Figure 3.1: Schematic of the bulk sheet material showing how specimens are cut at different orientations. Not to scale.

Various specimens were tested under different loading conditions. Tensile results were obtained by displacement controlled tests for both RD specimens and TD specimens. In addition, specimens from both directions were tested for creep and dwell

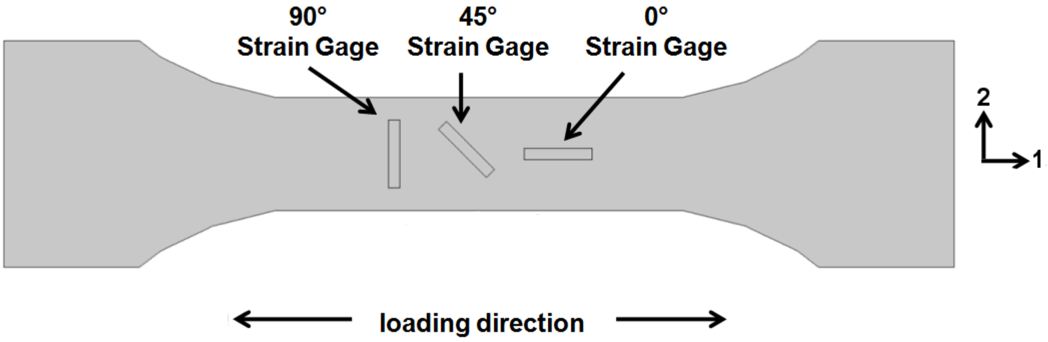

Figure 3.2: Schematic of a specimen showing strain gage placement and defining the specimen coordinate system (1-2) with 1 being the rolling direction. Not to scale.

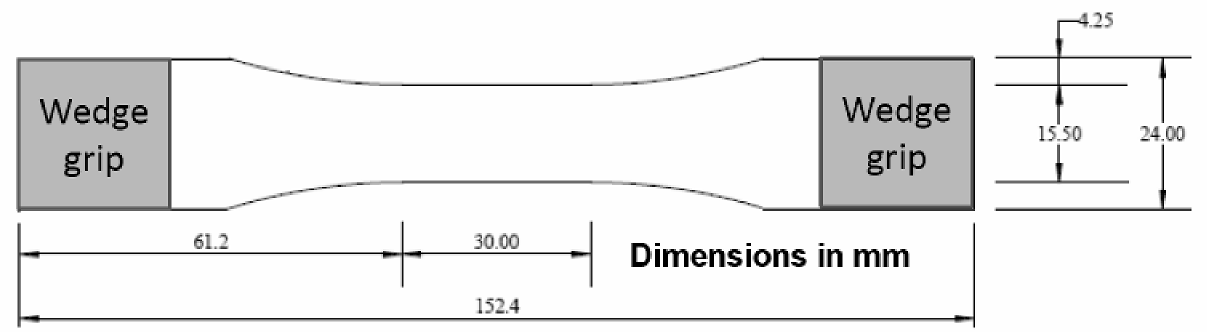

Figure 3.3: Specimen schematic to scale with dimensions in mm.

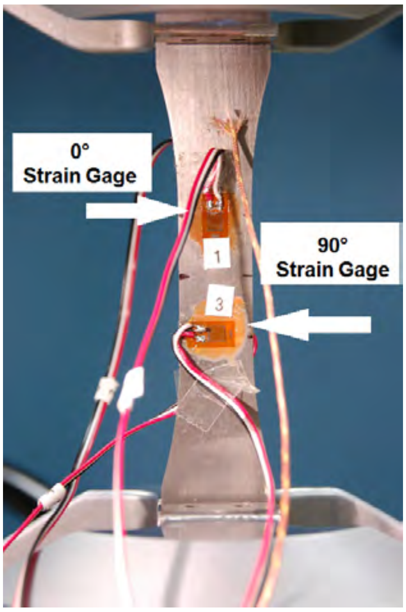

Figure 3.4: Close-up picture of a specimen fitted in rig for testing at AFRL/RX. Strain gages for this specimen are in the 0° and 90° orientations.

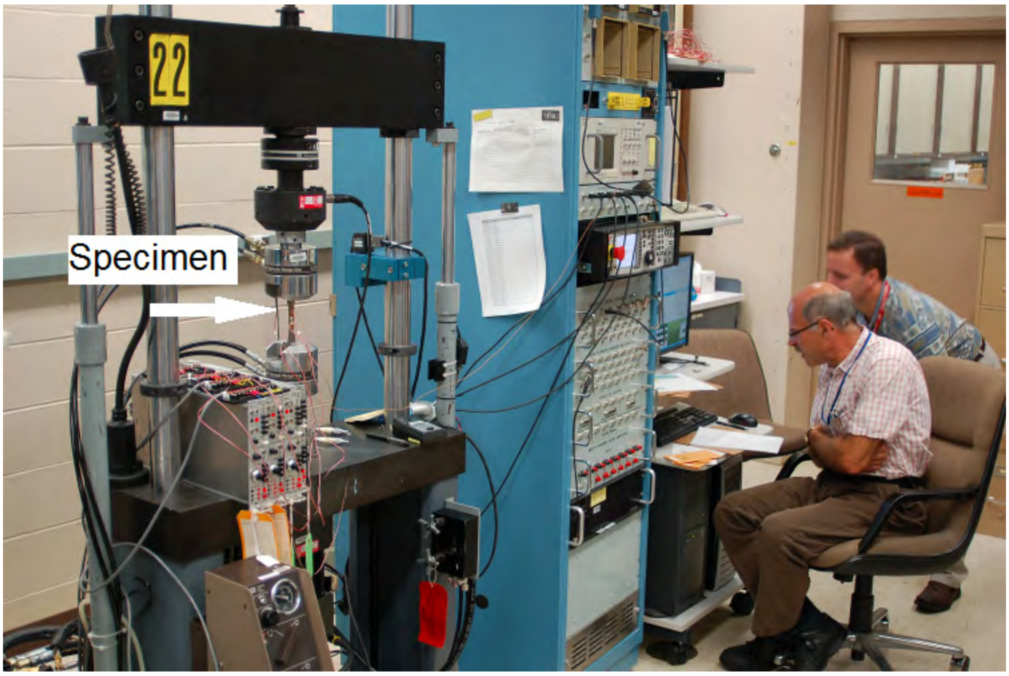

Figure 3.5: Picture of experimental set-up at AFRL/RX.

fatigue results through load controlled tests. The load controlled tests were conducted after the displacement controlled tests helped to determine yield strength. A number of loads were tested around the range of 95% of yield. Constant creep load and dwell loading pattern tests were conducted with the same maximum load for direct comparison of the dwell fatigue effect on mechanical response. See Table 3.1 for a detailed summary of the various test specimens. See Figure 3.6 for experimental tensile results and Figure 3.8 for experimental creep and dwell results. For the dwell experiments, strain values are reported at the midpoint during the dwell duration. See Figure 3.7 for a plot of the load pattern for 1 dwell cycle.

3.2 CPFEM Simulation of Polycrystalline Ti-3Al-2.5V

In order to accurately simulate the micromechanical response of polycrystalline materials, it is important to develop both a good microstructure model as well as a good micromechanical model. These separate but related aspects to the simulation are discussed in the following pages beginning with the microstructural simulation model.

3.2.1 3D Polycrystalline Microstructural Simulation and Mesh Generation

The following section discusses the 2D characterization and generation of 3D microstructure models from the 2D data. Section 2.1.1 gave a fuller set of details for the procedure while this particular section will focus on the extension of that procedure to include using EBSD scans from 3 orthogonal surfaces for a more precise representation of the morphological anisotropy of this rolled material.

Test Type	Spec. Orient.	Spec. ID	Max. Stress (MPa)	Dwell Time (s)	Stress Ratio, R	Ramp Rate (MPa/s)	Strain: 0°	Strain: 45°	Strain: 90°	Remarks
Tensile	RD	10-300	n/a	n/a	n/a	n/a	Yes	Yes	Yes	Interrupted
Tensile	RD	10-301	n/a	n/a	n/a	n/a	Yes	No	Yes	Interrupted
Tensile	TD	10-329	n/a	n/a	n/a	n/a	Yes	Yes	Yes	Interrupted
Tensile	TD	10-330	n/a	n/a	n/a	n/a	Yes	Yes	Yes	Interrupted
Tensile	TD	10-331	n/a	n/a	n/a	n/a	Yes	No	Yes	Interrupted
Creep	RD	10-302	600	n/a	n/a	20	Yes	No	Yes	Interrupted
Creep	RD	10-303	615	n/a	n/a	20	Yes	No	Yes	Interrupted
Creep	TD	10-332	615	n/a	n/a	20	Yes	No	Yes	Interrupted
Creep	TD	10-333	640	n/a	n/a	20	Yes	No	Yes	Interrupted
Dwell Fat.	RD	10-305	600	120	0.1	20.00	Yes	No	Yes	Interrupted
Dwell Fat.	RD	10-306	615	120	0.1	20.50	Yes	No	Yes	Failed
Dwell Fat.	TD	10-334	615	120	0.1	20.50	Yes	No	Yes	Interrupted
Dwell Fat.	TD	10-335	640	120	0.1	21.33	Yes	No	Yes	Failed

Table 3.1: Summary of specimen tests conducted at AFRL/RX.

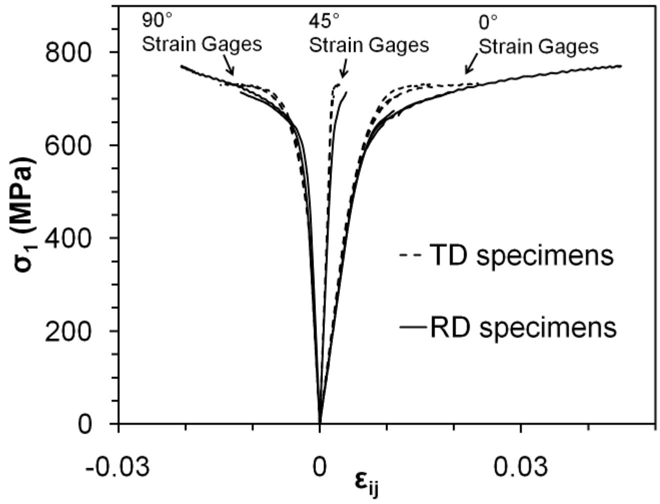

(a)

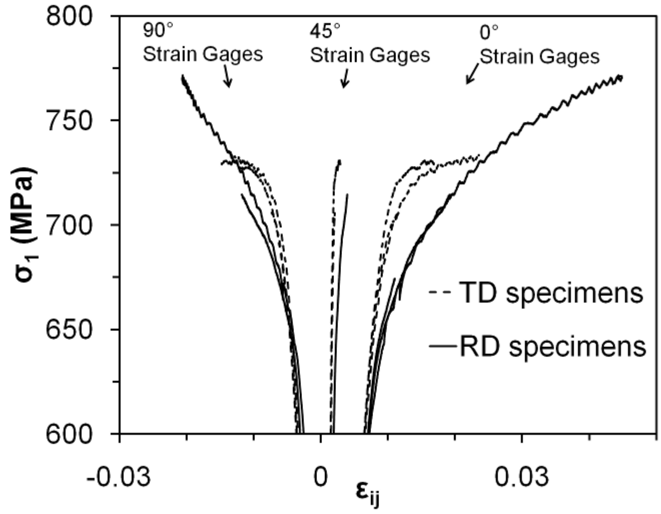

(b)

Figure 3.6: Experimental tensile results (full results (a) and a close-up (b)) where 0° strain gage corresponds to i=j=1, 90° strain gage corresponds to i=j=2, and 45° strain gage corresponds to i=1, j=2.

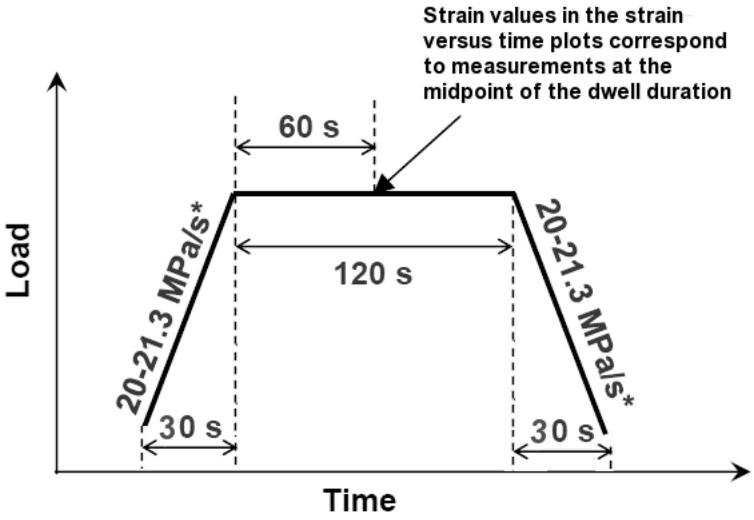

Figure 3.7: Dwell loading pattern for 1 cycle showing midpoint where data was collected past 10 cycles. Figure generated by AFRL/RX with some modification. *See Table 3.1 for specific ramp rates.

Microstructural Characterization of the α Ti-3Al-2.5V

Three EBSD scans of the Ti-3Al-2.5V material taken by AFRL/RX from 3 orthogonal surfaces were used to characterize the microstructure. A schematic of the rolled material labeling the three orthogonal surfaces was given in Figure 3.1 and the three EBSD scans are shown in Figure 3.9.

In contrast to the bi-modal α-β Ti-6Al-4V material studied in Chapter 2, this polycrystalline material is only composed of α phase which has an hcp crystal structure and associated slip systems (see Figure 2.2). Though this removes some of the modeling complexity (not needing to model the complicated transformed β phase), the rolled nature of this material gives rise to a pronounced crystallographic texturing as well as elongated grain shapes which, as will be shown, have a significant influence

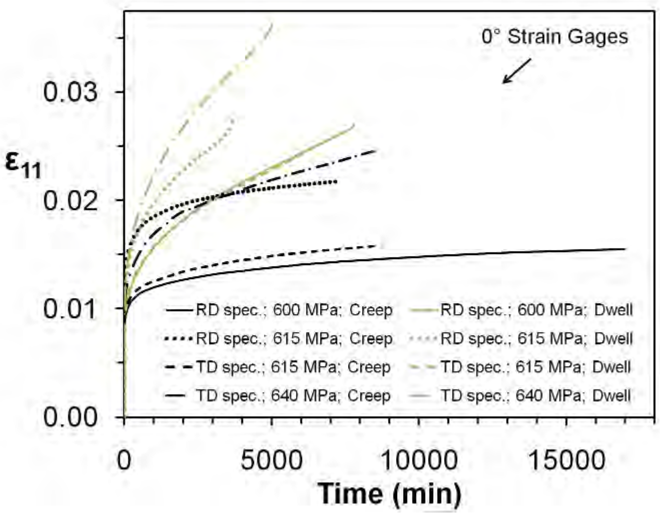

(a)

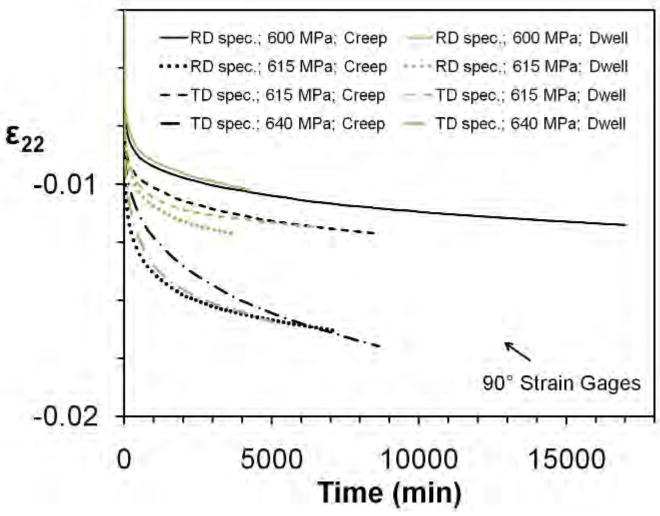

(b)

Figure 3.8: Experimental creep and dwell results for (a) 0° strain gages and (b) 90° strain gages.

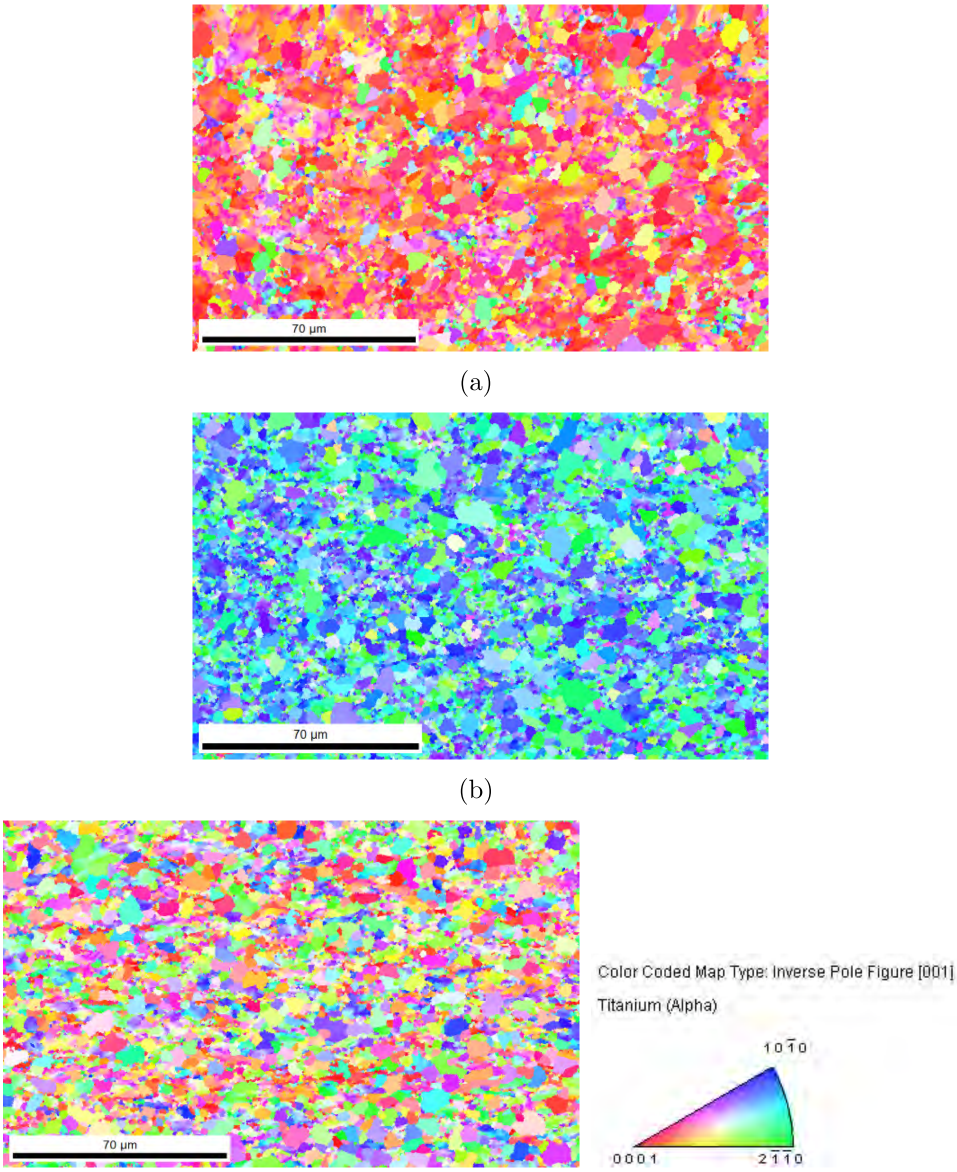

(a)

(b)

(c)

(d)

Figure 3.9: EBSD scans of (a) surface face, (b) transverse face, and (c) longitudinal faces; with (d) color legend.

on mechanical response properties. It is important that these features are accurately represented by the computational models.

Using the code described in [8], the EBSD scans from the three orthogonal faces were analyzed to determine a number of crystallographic and morphological microstructural characteristics including crystal size distribution, aspect ratio distribution and principal axis orientation distribution (assuming ellipsoidal-shaped grains), grain size versus number of neighbor distribution, crystallographic orientation distribution, misorientation distribution, and microtexture distribution.

Microstructural Simulation Procedure

Using a similar microstructural simulation procedure as described in Chapter 2, a representative synthetic microstructure is generated that is statistically equivalent to the real microstructure (as characterized by the statistics given in the previous section). As mentioned, the rolled nature of this material gives rise to deformed grain shapes. The rolled surface scan and aspect ratio analysis shows grains that have been ”flattened” while the longitudinal face shows grains that have been elongated in a ”bread-stick” fashion. One significant difference between the modeling work for this rolled material as compared to that for the Ti-6Al-4V material is that morphological aspect ratio data from the three orthogonal faces was matched in the full 3D synthetic microstructure. Grain shapes assumed to be elliptic in 2D are further assumed to be ellipsoidal in 3D with principal axis length distributions individually matched for each 2D face. Overlapping of grains and empty space is assigned to the nearest grains by an iterative process where statistics are monitored until convergence is reached and the entire cubic volume is filled with no overlapping. After the grain shapes have been placed and the volume has been filled, orientations are assigned to each grain based off a random sampling of the orientation distribution function and orientations are swapped until convergence is reached through an iterative process where misorientation and microtexture distribution errors are monitored.

A synthetic microstructure comprised of 534 grains was built in the fashion described above and can be considered statistically equivalent with respect to these important statistics. Chapter 2 has shown that the microstructure simulation algorithm converges with respect to grain size distribution for structures larger than approximately 300 grains. Figures 3.10 and 3.11 show the 534-grain structure from 4 viewpoints. Notice the difference in grain shapes from the 3 different faces of the microstructure. Visual inspection shows that the synthetic generator algorithm has faithfully reproduced a rolled microstructure.

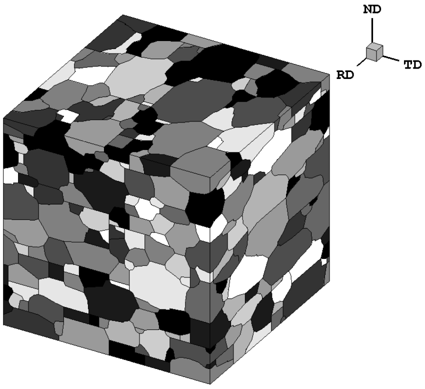

Figure 3.10: Voxelized volume for the 534-grain microstructure. The cube length dimension, l_0, is 24.6 μm.

Grain size distribution is another important microstructural feature that has a strong effect on mechanical properties especially as defined by the Hall-Petch relationship 2.14. Figure 3.12 shows the grain size distribution comparison for the real

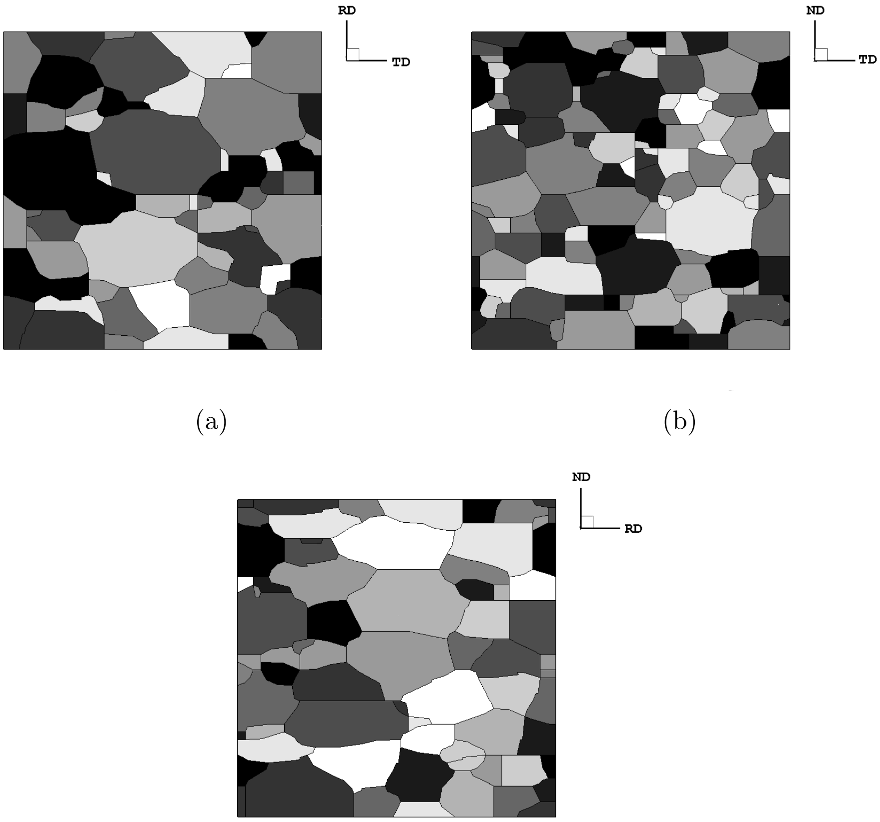

(a)

(b)

(c)

Figure 3.11: 2D views of the synthetic structure's (a) surface face, (b) transverse face, and (c) longitudinal face. Notice "flattened" shapes on surface face and elongated shapes on longitudinal face.

microstructure as compared to the synthetic microstructure. The version of the synthetic generator code available at the time had hard-coded standard deviation cut-offs that limited the maximum and minimum grain sizes that could be sampled from the lognormal curve fit. The grain size distribution based on volume fraction (Figure 3.12 (b)) helps visualize the pronounced effect of not matching the upper tail. The reason for the discrepancy is that the synthetic structure does not have as many of the largest sized grains as the real microstructure has. See Section 3.3.1 for a short discussion on a possible implication of this discrepancy. It is recommended that future work should investigate through a sensitivity the effect of not matching the upper tail of the grain size distribution.

Another very important microstructural statistic that effects mechanical response, is crystallographic orientation distribution. This characteristic is particularly important for the current material because of the anisotropic nature of hcp crystals (which comprise 100% of the structure) and the highly textured nature of the rolled material. Figure 3.13 gives a comparison of a (0002) pole figure for the sample data acquired from the EBSD scans and the 534 grains of the synthetic structure. A pole figure point density (PFPD) distribution comparison is included for a more quantitative comparison of the real structure's crystal orientation and the synthetic structure's crystal orientations. The crystallographic texture of the rolled Ti-3Al-2.5V is very similar to that seen for rolled commercially pure titanium as reported by Lutjering and Williams [25]. According to Collings [5], it is agreed that such a texture results from a competition between slip which rotates the basal poles toward the sheet normal, and twinning which tends to rotate them into the transverse direction. Hence,

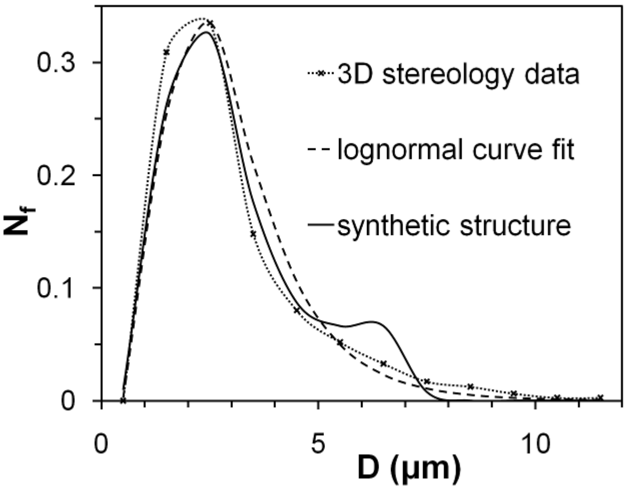

(a)

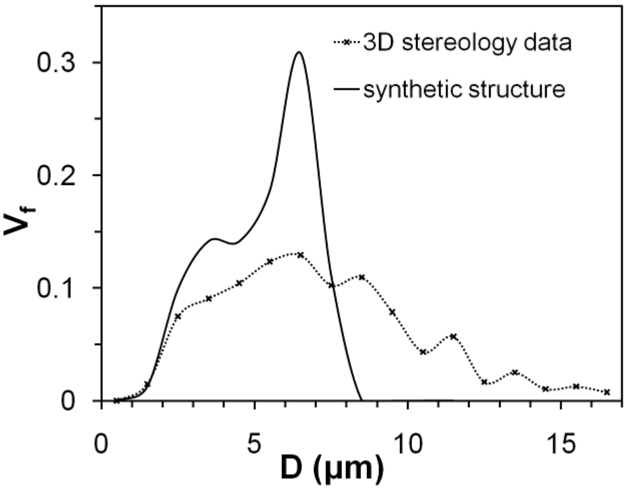

(b)

Figure 3.12: Grain size, D, distribution comparison based on (a) number fraction of grains (N_f) and (b) volume fraction of grains (V_f).

the (0002) pole figure for rolled titanium shows a concentration along the TD axis with some preference to the ND origin.

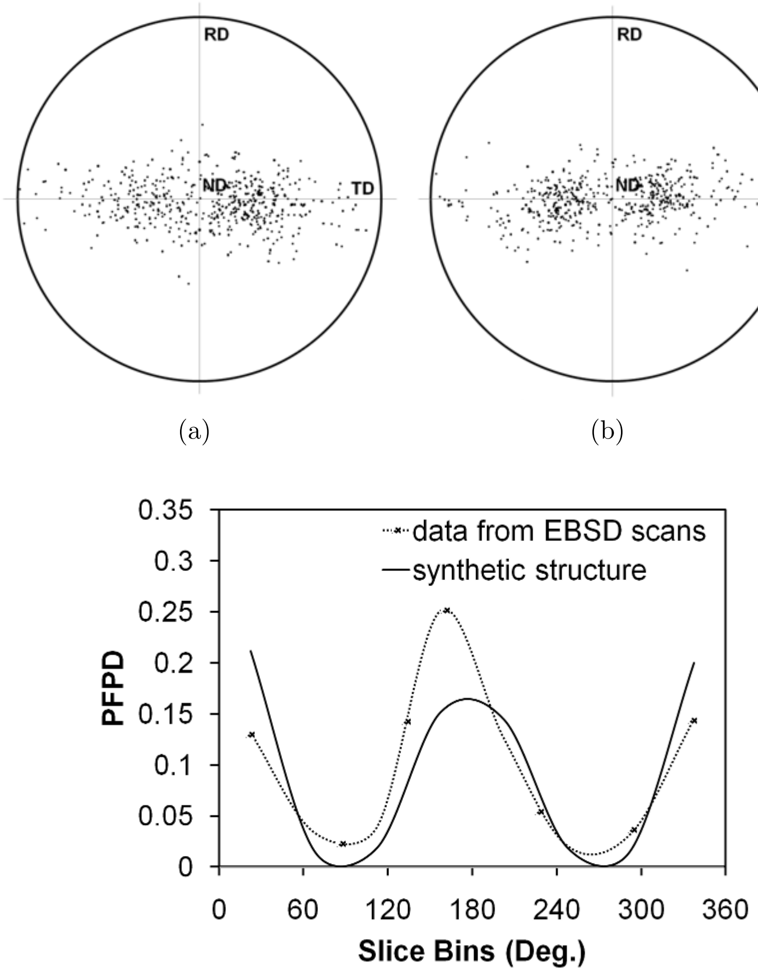

(a) (b)

(c)

Figure 3.13: α phase (0002) pole figures for (a) Sample data and (b) Synthetic structure as well as (c) pole figure point density (PFPD) distributions of the 2 pole figures for a more quantitative comparison of the crystallographic matching.

The synthetic generator code also matches the more local texturing metrics of misorientation distribution and microtexture distribution. See Figures 3.14 and 3.15

for a comparison of these statistics for the real structure and synthetic structure. Although not as important for this particular study, matching of these metrics becomes especially important for more local mechanical responses such as crack nucleation which is part of the proposed future work (see Chapter 4).

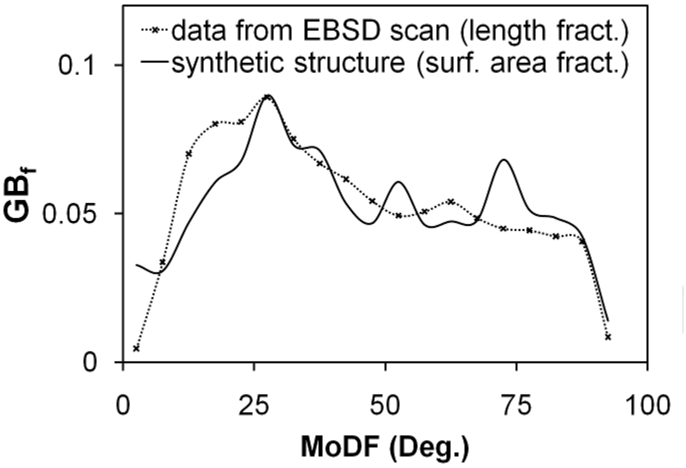

Figure 3.14: Misorientation distribution (MoDF) comparison. GB_f corresponds to either grain boundary length fraction or grain boundary surface area fraction.

Mesh Generation

The commercial software package Simmetrix [37] was used to mesh the voxelized volume generated by the synthetic structure generator code. The meshed structure consists of 151,474 four-noded tetrahedral elements and a total of 26,437 nodes. See Figure 3.16 (b) for a 3D view of the meshed structured. The mesh is checked for distorted elements and it is seen that less than 0.01% of the elements have an aspect ratio of 40 or higher. Section 2.1.1 has shown that for the Ti-6Al-4V material meshes of 500 or 600 grains that are meshed with similar resolution do not show any significant

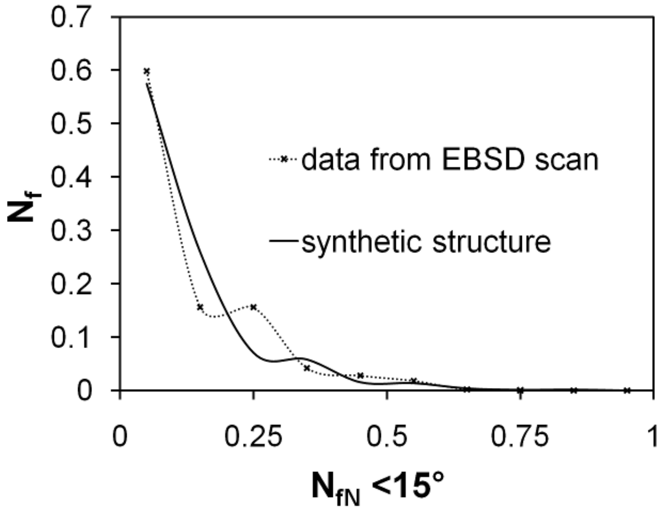

Figure 3.15: Microtexture distribution comparison where microtexture is defined by the number fraction of neighbors (N_{fN}) with misorientation less than 15°. N_f is the number fraction of grains.

mesh dependence when it comes to the volume averaged creep response. Because the current work is primarily concerned with volume averaged macroscopic responses, it is determined that the overall response will not be greatly affected by any mesh dependencies for this 534-grain structure.

This microstructure and mesh will be referred to in this work as *Microstructure A* or *MS-A* for short.

Simplified Microstructure for Model Updates, Sensitivity Studies and Parameter Calibration

Because of the large amount of computational expense of the meshed 534-grain synthetic structure (*MS-A*), a second simplified microstructure and mesh were developed with some justifiable simplifications for the purpose of performing model updates, sensitivity studies and parameter calibration.

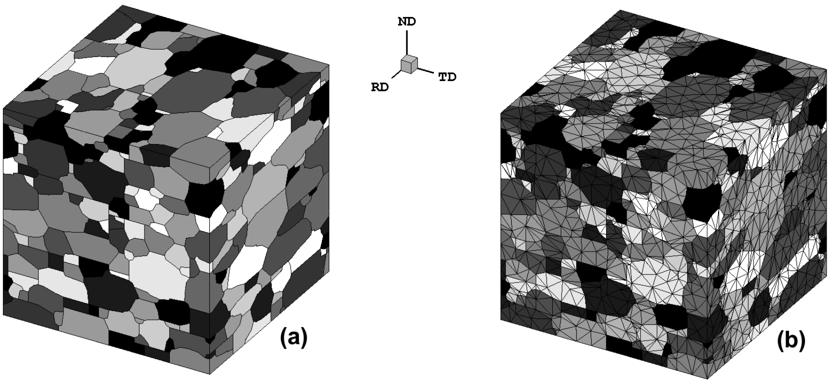

Figure 3.16: Voxelized volume (a) before and (b) after meshing for *MS-A*. The cube length dimension, l_0, is 24.6 μm.

A regular grid structure consisting of 2744 cubic grains with 8 tetrahedral elements per grain (for a total of 16464 elements) and 3375 nodes was generated. Orientations were assigned to the grains from a random sampling of orientations from the EBSD scan of the real microstructure producing a microstructure that was statistically equivalent in terms of the orientation distribution function.

According to an unpublished work by Anahid and Ghosh on a macroscopic yield surface model for titanium, it is not as important for the current work to consider the misorientation and microtexturing distributions. The effect of these characteristics on the macroscopic volume averaged constant strain rate and creep responses are not as pronounced as the relatively larger effects of grain size and orientation distribution. Again, as mentioned above, local effects that are highly dependent on local neighborhoods of grains are more sensitive to metrics such as misorientation and microtexturing. Crack nucleation models, for example, require these characteristics of the real sample to be accurately reproduced in any synthetic representations.

Since the scope of the current work is not focused on investigating local phenomena, matching of misorientation and texture distribution was neglected in this simplified microstructure for the model updates, parameter sensitivity study and calibration efforts.

Even though the finite element mesh has uniform grain sizes (1 μm cubes), the Hall-Petch size-effect as well as a newly developed aspect ratio dependence (see Section 3.2.2) is incorporated into the model by assigning different D values to the grains based on grain size and aspect ratio distributions of the real specimens. So, although the FEM mesh has grains of uniform size and shape, individual grains plastically deform differently from each other based on their D value assignment which corresponds directly to the real material.

In the simplified cubic grain structure for the D-aspect ratio dependence (discussed in Section 3.2.2), grains are oriented with their principal axes aligned with the rolling direction. This assumption is reasonable considering the ellipsoidal principal axes of the grains of the rolled structure are almost all aligned with the rolling direction with only slight variation as seen by visual inspection of the longitudinal face (Figure 3.11 (c)).

This microstructure and mesh will be referred to in this paper as *Microstructure B* or *MS-B* for short.

Table 3.2 summarizes the differences between the real microstructure and the synthetic structures *MS-A* and *MS-B*.

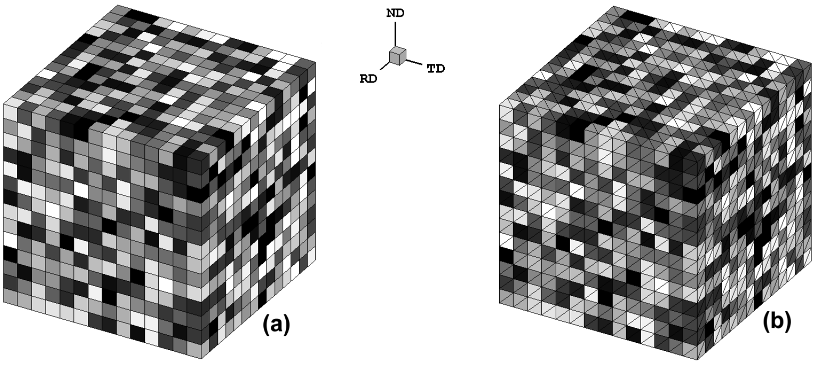

Figure 3.17: Regular grid model of *MS-B* ((a) before and (b) after meshing). The cube length dimension, l_0, is 14.0 μm.

	real	*MS-A*	*MS-B*
av. grain size (no. fract.), D	3.07 μm	3.08 μm	3.17 μm
st. dev. grain size (no. fract.)	1.77 μm	1.52 μm	1.50 μm
av. grain size (vol. fract.)	7.08 μm	5.19 μm	5.22 μm
st. dev. grain size (vol. fract.)	3.20 μm	1.52 μm	1.54 μm
max. grain size	16.8 μm	7.35 μm	7.37 μm
min. grain size	1.42 μm	0.71 μm	0.74 μm
vol. fract. α phase	100%	100%	100%
ellipsoid princ. axes matched?	n/a	yes	roll. dir.
orientation dist. matched?	n/a	yes	yes
misorientation dist. matched?	n/a	yes	no
texture dist. matched?	n/a	yes	no
mesh approx.	n/a	real. shapes	cubes
plastic property D approx.	n/a	equi. spheres	equi. ellip.
no. of grains	~2 billion	534	2,744
no. of elements	n/a	151,474	16,464
no. of elements per grain	n/a	~284	8
no. of nodes	n/a	26,437	3,375

Table 3.2: Summary of real microstructure compared with *MS-A* and *MS-B*.

3.2.2 Micromechanical Analysis of Simulated Polycrystalline Microstructures Using a Crystal Plasticity Constitutive Model

The isothermal, size-dependent and rate-dependent crystal plasticity finite-element model discussed in Section 2.1.2 is used along with an in-house parallel code to simulate the mechanical responses of *MS-A* and *MS-B*. The initial elastic and plastic parameters used were calibrated by previous single crystal work discussed in [13] and [7] where α Ti-6Al single crystal experimental data was available for calibration of individual slip system parameters. See Section 2.1.2 for initial values and Section 3.3.1 for the calibration efforts for this particular alloy. An implicit backward Euler time-integration scheme is used for the solution to the dynamic problem. An update to the CPFEM model is discussed and proposed in the following section.

Crystal Plasticity Constitutive Model Update to Include Grain Aspect Ratio Dependent Yielding

The constitutive equations governing the material behavior are all given in Section 2.1.2. The one notable difference being that the Ti-3Al-2.5V material has no transformed β colonies and therefore no bcc phase to model. This reduces the complexity of the constitutive equations; however, the rolled nature of this material gives rise to the need for an update to the model to account for grain aspect ratio dependency on the size effect for the hardness law, given previously as Equation 2.11. As mentioned, the slip system deformation resistance, g^α for each slip system is given a Hall-Petch-type size effect as $g^\alpha = g_0^\alpha + \frac{K^\alpha}{\sqrt{D^\alpha}}$. In previous work (including the work done for the Ti-6Al-4V material in Chapter 2), the value of the characteristic length scale, D^α assumed that each grain was spherical in shape. Therefore, there was no aspect ratio dependence governing the size effect on the g^α. This is a reasonable assumption as long as grain and colony shapes are relatively spherical in shape. However, for rolled materials, this assumption is no longer reasonable.

An update for the model is proposed and implemented which assigns different D^α values for each slip system (30 per grain for hcp crystals) based on the distance from the origin of an equivalent ellipsoid to a point on the ellipsoid's surface in the direction of slip multiplied by 2. A schematic of an ellipsoid is shown in Figure 3.18 with the new characteristic length given as D. This update to the model gives a more physical representation of the size effect on the yield property of individual grains which was originally developed based on the fact that grain boundaries impede dislocation motion.

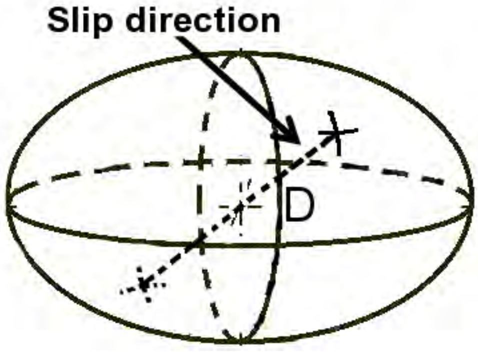

Figure 3.18: Schematic of an equivalent ellipsoid representing a grain showing how the new characteristic length scale, D^α, is constructed based on the intersection of a line from the origin in the slip direction to the intersection of the surface of the ellipsoid.

In actuality, for moderately rolled sheets of polycrystalline material where the grains are seen to be elongated by approximately 1.5 times (as is the case with the current material), it is seen that the effect of adding this dependence is not significant in the macroscopic volume averaged constant strain rate and creep response parameters. It is conjectured that this functionality would be very important for the more locally sensitive crack nucleation response of the material (see Chapter 4 for a discussion on future work). In order to see the effect of the model update in the macroscopic response, constant strain rate simulations were run on a microstructure where grains were elongated with an average a/b aspect ratio of 4 and a/c aspect ratio of 16, where a, b, and c correspond to the principal axis lengths. The microstructure was loaded in the rolling direction (the direction of the elongated grains). Comparison of the simulation results before and after the model update gave a 3.6% difference in yield strength (as measured by the 0.2% strain offset method). The aspect ratio dependent results predict a higher yield strength than that of the model which assumes equivalent spheres.

Boundary and Loading Conditions

Because of the limitation of micromechanical CPFEM to analyze microstructures with a maximum number of grains of the order of approximately 300-3000 grains, the absolute dimensions of the simulation models need to be limited to the order of about 50-150μm. This is much smaller than the actual experimental specimens which have gage lengths containing approximately 2 billion grains (as shown in Table 3.2) and dimensions reaching the order of centimeters (see Figure 3.3). Boundary conditions are used to approximate the behavior of the boundaries of these *micro*-cubes.

For the constant strain rate simulations, in order to suppress rigid body modes, symmetric constraint conditions are applied where the back faces of the cube are constrained as u_i=0 on the ith-face, where i goes from 1 to 3. Directions 1 and 2 represent specimen orientations in the RD and TD orientations while direction 3 is the sheet normal direction. The cube is free to move in all other directions. One of the outer faces is given a constant strain rate displacement boundary condition of $u_{ii}(t) = l_0(exp(\dot{\epsilon}^c_{ii}t) - 1)$, where l_0 is the initial dimension of the cube and $\dot{\epsilon}^c_{ii}$ is the applied constant strain rate which for these experiments is taken to be 9.76E-5 1/s. For the actual experiments, a constant stroke displacement rate of 6.16E-3 mm/s gave rise to an average strain rate of 7.63E-5 1/s for the elastic portion of the experiment and an average strain rate of 9.76E-5 1/s for the plastic portion of the experiment (the portion following yield). Different simulations were run using the average elastic rate for the entire simulation and the average plastic rate for the entire simulation and very little difference was seen in the macroscopic response; therefore, for simplification, the assumption of 9.76E-5 1/s as the strain rate for the entire simulation is taken to be reasonable. It is conjectured that for higher strain rate experiments that this assumption would no longer be valid and a more precise representation of the applied strain rates would be necessary to accurately model the experimental results. Constant strain rate simulations are run to about 5% total strain to ensure that the full tensile experiment range is simulated.

For the creep simulations, both symmetric boundary conditions (as discussed above) and minimum boundary conditions were used to ensure that boundary conditions were not affecting the macroscopic response too much. Minimum boundary conditions correspond to the back face of the cube being constrained from motion in the loading direction, 1 line on this same back face in the normal direction being constrained from motion in the non-loading direction (to constrain rotational motion about the loading direction), and 1 point at the origin being constrained in all three directions to restrain the rigid motion in the normal direction. It was seen for *MS-B* that using symmetric or minimum boundary conditions for the creep simulations did not affect the macroscopic response significantly. This verifies that we are not having a boundary condition dependence for these runs. For creep, constant loads are applied to one of the outer faces for about 334 hours.

3.3 CPFEM Simulation Results with Material Parameter Calibration Procedure and Model Validation Using Experimental Results

Using the material parameters calibrated for previous titanium alloys, initial tensile simulation results for the Ti-3Al-2.5V material did not match well. This is understandable because this is a different alloy with a different processing history. Yield strengths near 900 MPa were predicted for specimens of both RD and TD orientations while experimental results are nearer 600 MPa. In addition, the post-yield slopes were not matching well and the elastic portion of the simulations were also off by about 10%. Fortunately, the large amount of experimental data available allowed for some of the data to be used for calibration purposes.

The displacement controlled tensile experiments are used for calibration. Once the calibration is completed for the constant strain rate simulations using the tensile experimental results, validation of the model is achieved by predicting creep results using the calibrated model.

3.3.1 Material Parameter Calibration Using Displacement Controlled Experimental Data and Sensitivity Studies

Because of the anisotropic nature of the elastic and crystal plasticity constants, calibration efforts required the use of experimental data for both the RD and TD specimens to fully calibrate these directionally dependent constants. The hcp crystals exhibit different responses in the different directions and it was seen that the RD and TD specimens were sensitive to different material constants to different degrees. For visualization of slip family activity, Figure 3.19 gives the distributions of softness indices, SI, as defined by Equation 2.20 where here softness indices are shown for the specific slip families rather than for the softest slip system of the grain. "Activity" corresponds to values of softness index above 1 (the black vertical line in Figure 3.19). The simulations shows larger basal slip system activity in the TD specimens (red, dotted curve) than in the RD specimens where there is almost no basal activity (red, solid curve). In addition, the RD specimens (green, solid curve) show more prismatic activity than do the TD specimens (green, dotted curve). The difference in the plastic response of these slip systems is what largely accounts for the different macroscopic responses in the polycrystalline material. For this reason, it would not be possible to calibrate using RD specimen data and then predict the TD specimen response accurately.

Elastic Parameter Calibration

The elastic parameters were calibrated through sensitivity studies where the 5 independent constants were varied while holding all others constant. Using the sensitivity study results, the parameters were tweaked until the elastic portion of the constant strain rates simulations for both RD and TD specimens matched tensile experimental results. Table 3.3 gives the final calibrated results and Table 3.4 shows a comparison of the experimental elastic properties versus the simulated properties (before and after calibration).

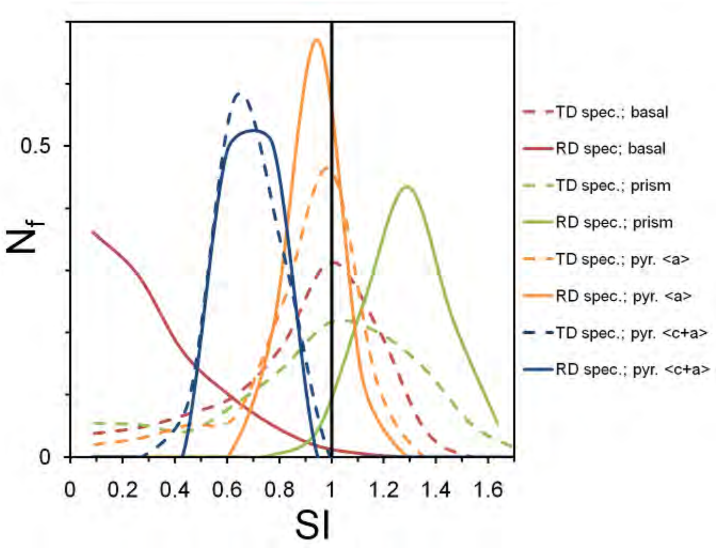

Figure 3.19: Distribution of softness index ($SI \equiv SF^{\alpha} * YS/g_0^{\alpha}$) of slip families. N_f is the number fraction of grains. Values of SI above 1 correspond to slip activity.

C_{ij} parameter	Value (GPa)
C_{11}=C_{22}	162.2
C_{33}	95.6
C_{12}=C_{21}	83.9
C_{13}=C_{31}=C_{23}=C_{32}	204.0
C_{44}	C_{11}-C_{12}
C_{55}=C_{66}	87.0
Other C_{ij}	0

Table 3.3: Calibration of the Ti-3Al-2.5V transversely isotropic elastic parameter tensor.

	Exp.		Sim. Pre-calib.		Sim. Post-calib.	
spec. orient.	E_{ii} (GPa)	ν_{ii}	E_{ii} (GPa)	ν_{ii}	E_{ii} (GPa)	ν_{ii}
RD (i=1)	102	0.390	109	0.376	102	0.383
TD (i=2)	111	0.417	121	0.416	110	0.412

Table 3.4: Elastic response parameter comparison for experiments with the simulations before and after calibration.

Crystal Plasticity Parameter Calibration

Crystal plasticity parameter calibration was accomplished by the aid of a wide range of sensitivity studies performed on the *MS-B* microstructure. Studied parameters include: h_0, $\dot{\tilde{\gamma}}$, m, q_{ab}, n, r, and initial slip system hardness parameters, g_0^α, for slip in the basal <a>, prismatic <a>, pyramidal <c>, and pyramidal <c+a>directions. Additionally, a small model update was made where the $\tilde{g}$ saturation hardness parameter is defined as a scaled up value from the size-effect-modified g_0 values given as $\hat{g_0}$. This update is a safe guard that the size-effect modifications on the g_0^α values do not create an unphysical situation where the saturation value is actually less than the initial hardness of the slip system. This was seen to occur with the previous model causing an unphysical softening of slip systems as plastic deformation increased.

Table 3.5 gives the previously calibrated values as well as the calibrated values for *MS-A*. When the calibrated values for *MS-A* were applied to *MS-B*, the results did not match as well as would be desired. The reason for this can be explained by the differences between these 2 microstructures as outlined in Table 3.2. A small amount of additional calibration was required to match the simulation results for *MS-B* (as shown in the last column of 3.5). This issue was not seen in an unpublished work by Anahid and Ghosh based on a comparison of a cube-shaped grain model and a real-shaped grain model of the Ti-6Al-4V alloy discussed in Chapter 2. It is conjectured that modeling of the actual grain shapes has a pronounced effect on the CPFEM results in this case because of the elongated grain shapes for the current rolled material.

Figure 3.20 shows the *MS-A* constant strain rate simulation results after calibration as compared with experimental results and Figure 3.21 gives the results for *MS-B*

		Prev.	Ti-3Al-2.5V	
Parameter	Unit	Calib.	*MS-A*	*MS-B*
g_0 basal <a>	(MPa)	385.0	239.0	199.2
g_0 prism <a>	(MPa)	365.0	175.6	146.4
g_0 pyr. <a>	(MPa)	n/a	289.1	240.9
g_0 pyr. <c+a>	(MPa)	623.3	456.1	380.1
$\tilde{g}$ basal <a>	(MPa)	450.0	$\hat{g}_0$*1.2	$\hat{g}_0$*1.2
$\tilde{g}$ prism <a>	(MPa)	550.0	$\hat{g}_0$*1.6	$\hat{g}_0$*1.6
$\tilde{g}$ pyr. <a>	(MPa)	1650.0	$\hat{g}_0$*1.6	$\hat{g}_0$*1.6
$\tilde{g}$ pyr. <c+a>	(MPa)	450.0	$\hat{g}_0$*1.6	$\hat{g}_0$*1.6
h_0 basal <a>		100.0	100.0	100.0
h_0 prism <a>		100.0	100.0	100.0
h_0 pyr. <a>		100.0	100.0	100.0
h_0 pyr. <c+a>		100.0	100.0	100.0
$\dot{\tilde{\gamma}}$		0.0023	0.0023	0.0023
m		0.02	0.02	0.02
n		0.01	0.01	0.01
r		0.1	0.1	0.1

Table 3.5: Calibration of Ti-3Al-2.5V crystal plast. parameters.

as compared with experimental results. The elastic portion of these curves for both RD and TD specimens matches almost perfectly. Yield strengths also look good for both specimen directions with the RD specimens showing a lower yield point consistent with experiments and the TD specimens showing a slightly higher yield point consistent with experiments. Post-yield slopes leave a little to be desired when it comes to matching with the experiments (at least for 1 of the 2 directions). For *MS-A* the post-yield slope for the RD specimen look almost perfect; however, for the TD specimens the results do not match well. Conversely, for *MS-B* the post-yield slope for the TD specimen looks good while the RD specimen result is not as good. It is observed that after about 1-3% strain that the post-yield slopes for specimens of both orientations converge to the same value in the simulations, while in the experiments this is not the case. The RD and TD specimens continue to show a marked slope difference past 1-3% strain. An attempt was made to match this anisotropic post-yield response by calibration of individual plastic slip system parameters. Though good agreement could be achieved by modifying h_0 values by 72 times their original values, such a large adjustment of previously calibrated parameters did not seem safe. Further study is recommended. Particularly needful would be to look into the physical mechanisms which give rise to such a dramatic difference in post-yield slopes for the 2 specimen orientations. It is probable that the current models are not able (without a extremely dramatic adjustment of plastic parameters) to capture the highly anisotropic post-yield slope difference past 1-3% strains. It is also probable that error has been introduced because the grain size validation was conducted based on visual inspection of the grain size distribution based on number fraction instead of volume fraction. A further cause for error could be in the ODF matching (as seen in the PFPD plot of Figure 3.13) and sensitivities to perturbations in the ODF should be studied to determine if indeed the ODF matching needs to be improved.

3.3.2 Model Validation Using Load Controlled Experimental Data

Model validation is achieved by using the calibrated model to predict the creep response of the material under different load levels and specimen orientations for *MS-B*. Figure 3.22 shows the experimental results as compared to the simulation results for *MS-B*.

Dwell results do not match well with the experimental data and are not shown. The current model has no parameter or equation in place to capture the mechanism

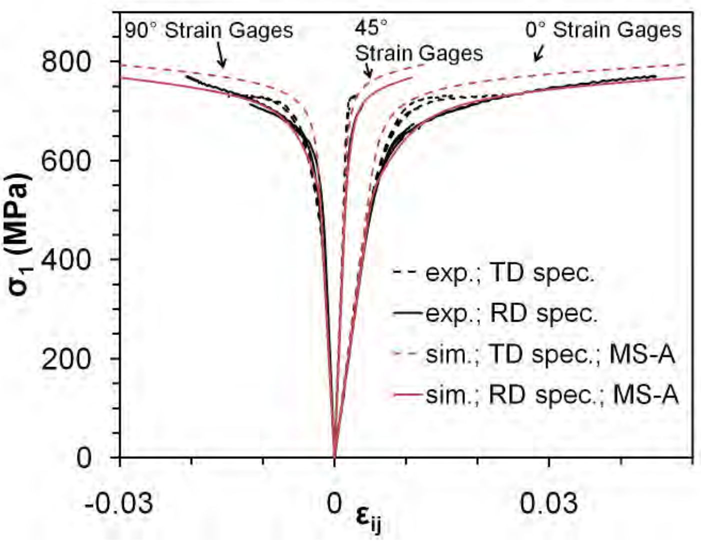

(a)

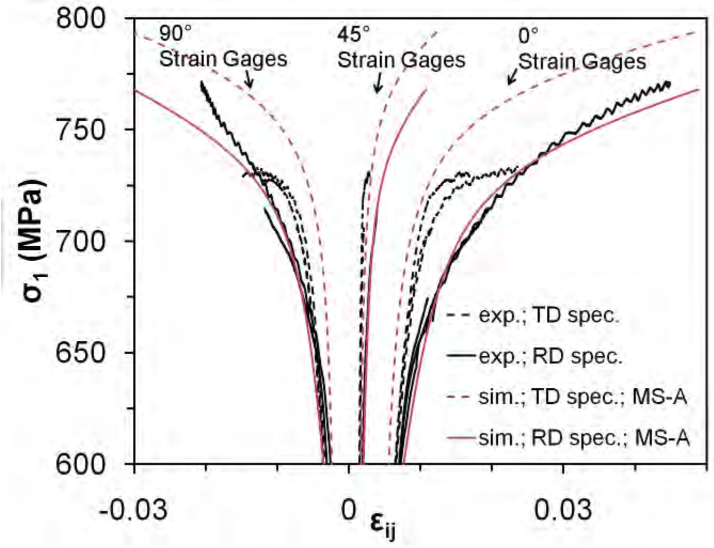

(b)

Figure 3.20: Comparison of experimental tensile results with constant-strain rate simulation results for *MS-A* (full results (a) and a close-up (b)) where 0° strain gage corresponds to i=j=1, 90° strain gage corresponds to i=j=2, and 45° strain gage corresponds to i=1, j=2.

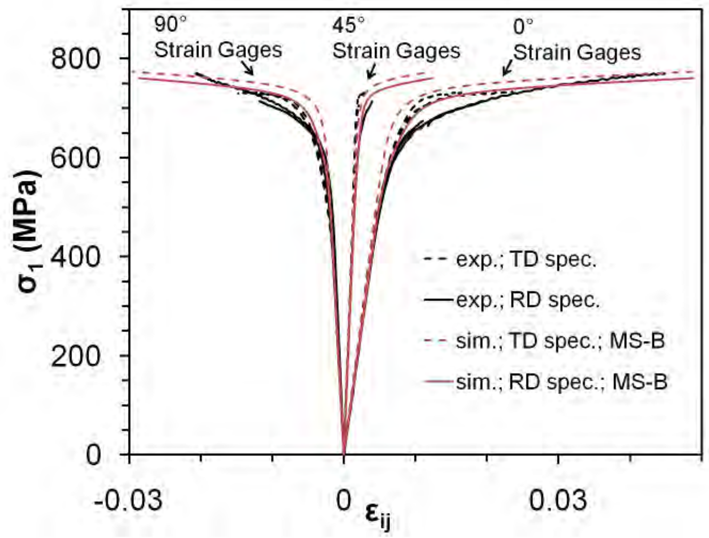

(a)

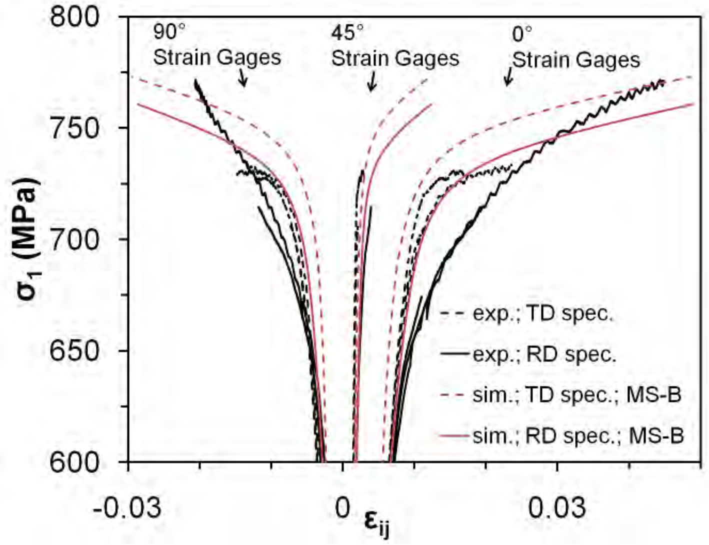

(b)

Figure 3.21: Comparison of experimental tensile results with constant-strain rate simulation results for *MS-B* (full results (a) and a close-up (b)) where 0° strain gage corresponds to i=j=1, 90° strain gage corresponds to i=j=2, and 45° strain gage corresponds to i=1, j=2.

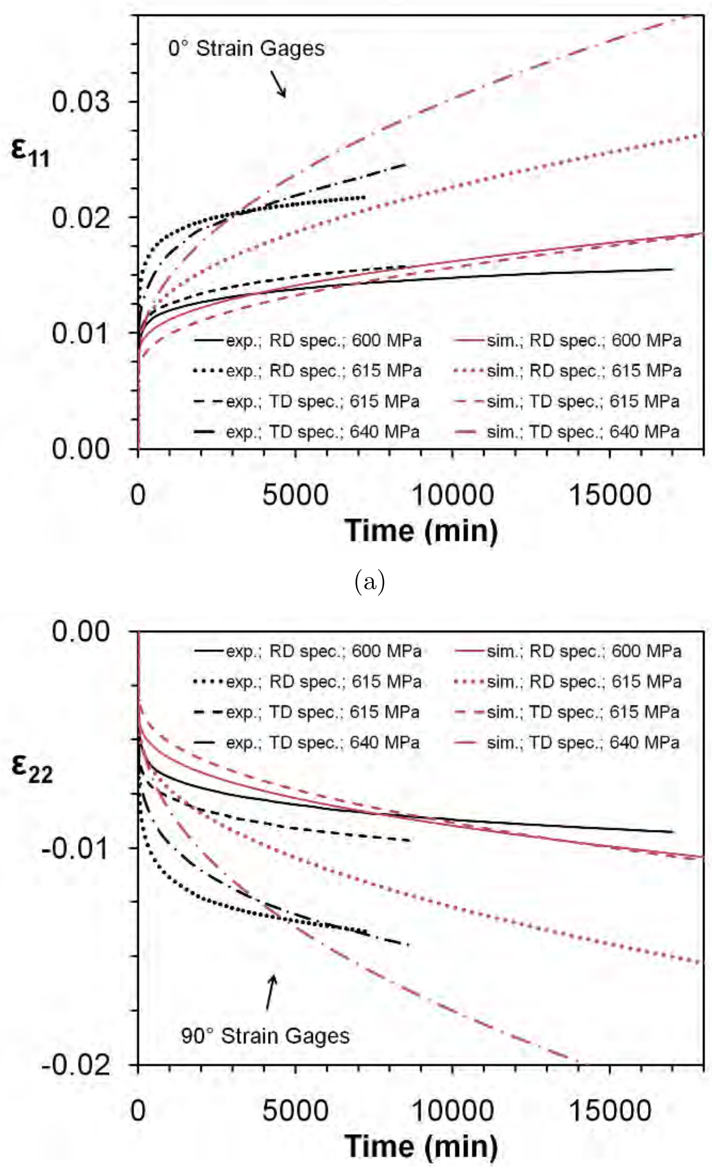

(a)

(b)

Figure 3.22: Creep validation for (a) 0° strain gages and (b) 90° strain gages.

that gives rise to such a dramatic difference in plastic strain for the dwell loading versus the creep loading (as seen in Figure 3.8). It is conjectured that the reason the dwell experiments have such a high plastic strain as compared to the creep experiments of the same maximum load is due to dislocation motion during the unloading and reloading portion of the dwell cycle. During unloading and reloading, it is probable that there is a relaxation effect where dislocations piled up next to grain boundaries tend to diffuse into the center of grains finding a minimum energy configuration. This corresponds to the grains being able to see more plasticity upon the next dwell hold. This is a possible reason for the added plastic strain for the dwell loading experiments as compared to the creep loading experiments. The current model does not include any dependence on an unloading/reloading cycle that would allow for this relaxation and the associated softening. This could be included in future work which could take advantage of the large amount of dwell experimental data presented here.

Chapter 4: Conclusions and Future Work

This thesis demonstrates that a complete procedure is in place to study a large number of material microstructures by computational means. A relatively efficient data collection and processing procedure and a robust synthetic microstructure generating program combined with a meshing software and crystal plasticity based finite element analysis program were integrated to yield a useful computational tool. This procedure is able to accurately predict the macroscopic constant strain rate response as well as the primary and secondary macroscopic creep response of important high-performance titanium alloys. Because the model calculates the elastic-plastic response of individual grains along specific slip systems, insight is gained into the "inner workings" of the material response on a grain level. In addition, large sets of model microstructures with vastly different characteristics were created and used to develop functional forms that relate microstructural parameters to responses such as yield strength, creep parameters, and Ramberg-Osgood parameters. The proposed model for yield strength as a function of α lath thickness is validated against a previous published regression model based off 75 separate experiments.

In addition, a CPFEM model update has been proposed and implemented that provides strides towards modeling plasticity more realistically in grains with elongated shapes. Because of the large amount of experimental data available for specimens of different orientations, the current models were able to be calibrated as well as validated by predicting the creep response under different loads and specimen orientations. The current model is not able to capture the dwell fatigue response; however, the experimental data reported here could be used in the future to develop a model that captures this pronounced dwell effect.

Future work could also consider time to failure under fatigue loading as a response parameter. The "weakest link," local nature of fatigue failure would require the introduction of probabilistic methods and the large times to failure of many materials requires multi-scaling techniques but nonetheless the groundwork is laid for developing these important functional dependencies.

In addition, the functional dependencies developed in this work are a step towards helping to remove the industry's heavy reliance on expensive experiments as well as their need to perform expensive crystal plasticity simulations. The sensitivity analyses performed here also give feedback to those responsible for advancing the accuracy and efficiency of materials characterization as to the microstructural features that are the most critical to particular mechanical responses. This information can be valuable to the end that time and energy can be focused on advancing the efficiency and accuracy of characterization of the features most crucial to particular response variables.

Bibliography

[1] S. Balasubramanian and L. Anand. *Acta Materialia*, 50:133–148, 2002.

[2] Max Blosser. Fundamental Modeling and Thermal Performance Issues for Metallic Thermal Protection System Concept. *Journal of Spacecraft and Rockets*, 41(2):195–206, 2004.

[3] Max L. Blosser. Development of Metallic Thermal Protection Systems for the Reusable Launch Vehicle. *NASA Technical Memorandum 110296*, 1996.

[4] H. P. Chu. *Journal of Materials*, 5:633–642, 1970.

[5] E.W. Collings. *The physical metallurgy of titanium alloys.* ASM series in metal processing. American Society for Metals, 1984.

[6] P. Collins. *A combinatorial approach to the development of composition-microstructure-property relationships in titanium alloys using directed laser deposition.* PhD thesis, The Ohio State University, 201 West 19th Avenue, Columbus, OH 43210, 2004.

[7] Dhyanjyoti Deka, Deepu S. Joseph, Somnath Ghosh, and Michael J. Mills. *Metallurgical and Materials Transactions A*, 37(5):1371–1388, 2006.

[8] M. Groeber. *Development of an automated characterization-representation framework for the modeling of polycrystalline materials in 3D.* PhD thesis, The Ohio State University, 201 West 19th Avenue, Columbus, OH 43210, 2007.

[9] M. Groeber, S. Ghosh, M. Uchic, and D. Dimiduk. *Acta Materialia*, 56:1257–1273, 2008.

[10] M.A. Groeber, B.K. Haley, M.D. Uchic, D.M. Dimiduk, and S. Ghosh. *Materials Characterization*, 57:259–273, 2006.

[11] E O Hall. *Proceedings of the Physical Society. Section B*, 64(9):747–753, 1951.

[12] S. Harren, T. C. Lowe, R. J. Asaro, and A. Needleman. *Philosophical Transactions of the Royal Society of London. Series A, Mathematical and Physical Sciences*, 328(1600):443–500, 1989.

[13] V. Hasija, S. Ghosh, M. Mills, and D. Joseph. *Acta Materialia*, 51:4533–4549, 2003.

[14] V Hasija, S Ghosh, M J Mills, and D Joseph. *Acta Materialia*, 51(15):4533–4549, 2003.

[15] R W Hayes, G B Viswanathan, and M J Mills. *Acta Materialia*, 50(20):4953–4963, December 2002.

[16] D. Joseph. *Wavelet Based Dual Time Scale Method for the Analysis of Cyclic Deformation of Polycrystalline Materials*. PhD thesis, The Ohio State University, 201 West 19th Avenue, Columbus, OH 43210, 2010.

[17] T Kanit. Determination of the size of the representative volume element for random composites: statistical and numerical approach. *International Journal of Solids and Structures*, 40(13-14):3647–3679, 2003.

[18] S. Kar. *Modeling of Mechanical Properties in Alpha/Beta-Titanium*. PhD thesis, The Ohio State University, 201 West 19th Avenue, Columbus, OH 43210, 2005.

[19] S. Kar, T. Searles, E. Lee, G. Viswanathan, J. Tiley, R. Banerjee, and H. Fraser. *Metallurgical and Materials Transactions A*, 37:559–566, 2006.

[20] S Karthikeyan, G B Viswanathan, P I Gouma, Vijay K Vasudevan, Y W Kim, and M J Mills. *Materials Science and Engineering A*, 329-331:621–630, June 2002.

[21] M. Kothari and L. Anand. *J. Mech. Phys. Solids*, 46(1):51–83, 1998.

[22] E Lauridsen, S Schmidt, S Nielsen, L Margulies, H Poulsen, and D Jensen. *Scripta Materialia*, 55(1):51–56, 2006.

[23] E. Lee. *Microstructure evolution and microstructure: Mechanical properties relationships in alpha-beta Titanium Alloys*. PhD thesis, The Ohio State University, 201 West 19th Avenue, Columbus, OH 43210, 2004.

[24] J.D. Lubahn and R.P. Felgar. *Wiley series on the Science and Technology of Materials: Plasticity, Creep, Metals*, 1961.

[25] G. Lutjering and J. Williams. *Titanium*. Springer, 2003.

[26] Ryan J Morrissey, Reji John, Mark Ruddell, Phil Blosser, and Dennis Buchanan. TEST SYSTEM FOR ELEVATED TEMPERATURE CHARACTERIZATION OF THIN METALLIC FOILS (PREPRINT). *PREPRINT*, 2010.

[27] MSC Software Corporation, Santa Ana, CA. *MSC Marc-Mentat*, 2009.

[28] T Neeraj, D H Hou, G S Daehn, and M J Mills. *Acta Materialia*, 48, 2000.

[29] T Neeraj and M J Mills. *Materials Science and Engineering A*, 321:415– 419, 2001.

[30] N. J. Petch. *J Iron Steel Inst*, 174:25, 1953.

[31] W. Ramberg and W. Osgood. *National Advisory Committee For Aeronautics*, 902, 1943.

[32] V. Randle, G. Rohrer, and Y. Hu. *Scripta Materialia*, 58:183–186, 2008.

[33] D J Rowenhorst and P W Voorhees. *Metallurgical and Materials Transactions A*, 36(August):2127–2135, 2005.

[34] J. C. Russ and R. T. Dehoff. *Practical Stereology*. Plenum Press, 2nd edition edition, 1999.

[35] M F Savage, T Neeraj, and M J Mills. *Metallurgical and Materials Transactions A*, 33(March), 2002.

[36] T. Searles. Microstructural characterization of the α/β titanium alloy Ti-6Al-4V. Master's thesis, The Ohio State University, 201 West 19th Avenue, Columbus, OH 43210, 2005.

[37] Simmetrix Inc., Clifton Park, NY 12065. *MeshSim User's Guide*, 2003.

[38] S Suri, T Neeraj, G S Daehn, D H Hou, J M Scott, R W Hayes, and M J Mills. *Materials Science and Engineering A*, 236:996–999, 1997.

[39] S Suri, G B Viswanathan, T Neeraj, D H Hou, and M J Mills. *Acta Metallurgica*, 47(3), 1999.

[40] J. Tiley. *Modeling of microstructure property relationships in Ti-6Al-4V*. PhD thesis, The Ohio State University, 201 West 19th Avenue, Columbus, OH 43210, 2002.

[41] G. Venkataramani, K. Kirane, and S. Ghosh. *International Journal of Plasticity*, 24:428–454, 2008.

[42] G. Venkatramani, S. Ghosh, and M. Mills. *Acta Materialia*, 55:3971–3986, 2007.

[43] G Viswanathan, S Karthikeyan, R W Hayes, and M J Mills. *Acta Materialia*, 50(20):4965–4980, December 2002.

[44] B. Welk. Microstructural and property relationships in titanium alloy ti-5553. Master's thesis, The Ohio State University, 201 West 19th Avenue, Columbus, OH 43210, 2010.

[45] H Yoshimura. *Journal of Alloys and Compounds*, 293-295(1-2):858–861, 1999.